Monthly Notices of the ROYAL ASTRONOMICAL SOCIETY

MNRAS **491,** 3586–3605 (2020) doi:10.1093/mnras/stz2906
Advance Access publication 2019 October 18

Gravity-mode period spacings and near-core rotation rates of 611 γ Doradus stars with *Kepler*

Gang Li,[1,2]★ Timothy Van Reeth,[1,2,3] Timothy R. Bedding ,[1,2]★ Simon J. Murphy,[1,2] Victoria Antoci ,[2] Rhita-Maria Ouazzani[4] and Nicholas H. Barbara[1,2]

[1]*Sydney Institute for Astronomy (SIfA), School of Physics, University of Sydney, NSW 2006, Australia*
[2]*Stellar Astrophysics Centre, Department of Physics and Astronomy, Aarhus University, Ny Munkegade 120, DK-8000 Aarhus C, Denmark*
[3]*Institute of Astronomy, KU Leuven, Celestijnenlaan 200D, B-3001 Leuven, Belgium*
[4]*LESIA, Observatoire de Paris, PSL Research University, CNRS, Sorbonne Universités, UPMC Univ. Paris 06, Univ. Paris Diderot, Sorbonne Paris Cité, 5 place Jules Janssen, F-92195 Meudon, France*

Accepted 2019 October 13. Received 2019 October 1; in original form 2019 August 10

ABSTRACT

We report our survey of γ Dor stars from the 4-yr *Kepler* mission. These stars pulsate mainly in g modes and r modes, showing period-spacing patterns in the amplitude spectra. The period-spacing patterns are sensitive to the chemical composition gradients and the near-core rotation, hence they are essential for understanding the stellar interior. We identified period-spacing patterns in 611 γ Dor stars. Almost every star pulsates in dipole g modes, while about 30 per cent of stars also show clear patterns for quadrupole g modes and 16 per cent of stars present r-mode patterns. We measure periods, period spacings, and the gradient of the period spacings. These three observables guide the mode identifications and can be used to estimate the near-core rotation rate. We find many stars are hotter and show longer period-spacing patterns than theory. Using the traditional approximation of rotation (TAR), we inferred the asymptotic spacings, the near-core rotation rates, and the radial orders of the g and r modes. Most stars have a near-core rotation rate around 1 d^{-1} and an asymptotic spacing around 4000 s. We also find that many stars rotate more slowly than predicted by theory for unclear reasons. 11 stars show rotational splittings with fast rotation rates. We compared the observed slope–rotation relation with the theory and find a large spread. We detected rotational modulations in 58 stars and used them to derive the core-to-surface rotation ratios. The interiors rotate faster than the cores in most stars, but by no more than 5 per cent.

Key words: stars: oscillations – stars: rotation.

1 INTRODUCTION

Rotation affects the transport of chemical elements and angular momentum in stars, so it changes stellar structure and evolution (e.g. Maeder 2009; Mathis et al. 2013). However, the theoretical description of rotation is still a matter of debate. For example, the observed core-to-surface rotation rate ratios in red giants are smaller than predicted by theory (see e.g. Eggenberger, Montalbán & Miglio 2012; Mosser et al. 2012; Ceillier et al. 2013; Fuller, Piro & Jermyn 2019). For A- and F-type main-sequence stars, the typical value of the projected surface rotation velocity is around 100 km s^{-1} and increases with effective temperature (e.g. Fukuda 1982; Abt & Morrell 1995; Groot, Piters & van Paradijs 1996; Royer, Zorec & Gómez 2007). Hence, the effect of rapid rotation must be treated properly.

Stellar oscillations are a powerful tool to investigate the stellar interior. We focus on γ Doradus stars, which are A- to F-type main-sequence stars with typical masses from 1.4 to 2.0 $M_\odot$ (e.g. Kaye et al. 1999; Van Reeth, Tkachenko & Aerts 2016). The pulsations of γ Dor stars are gravity modes with high radial order ($20 \lesssim n \lesssim 100$) low degree ($l \lesssim 4$) with typical pulsation period from 0.3 to 3 d (Balona, Krisciunas & Cousins 1994; Kaye et al. 1999; Saio et al. 2018b; Van Reeth et al. 2018; Li et al. 2019b). Gravity modes have their highest mode energy in the near-core regions (e.g. Triana et al. 2015; Van Reeth et al. 2016). Therefore, γ Dor stars allow us to investigate the stellar interior. The excitation mechanism of γ Dor stars is still in debate. Guzik et al. (2000) and Dupret et al. (2005) reported that the g-mode pulsations are excited by the convective flux blocking mechanism that operates at the base of the envelope convection zone. Xiong et al. (2016) found that the radiative κ mechanism plays a major role in warm γ Dor stars while

★ E-mail: gali8292@uni.sydney.edu.au (GL); tim.bedding@sydney.edu.au (TRB)

the coupling between convection and oscillations is dominant in cool stars. Turbulent thermal convection is a damping mechanism that gives rise to the red edge of the instability strip. Grassitelli et al. (2015) pointed out that turbulent pressure fluctuations may contribute to the γ Dor phenomenon. The instability strip of γ Dor stars is located between the solar-like stars and the δ Scuti stars, overlapping with the red edge of the δ Scuti instability strip (Dupret et al. 2005; Bouabid et al. 2009, 2013). Hence some γ Dor stars show both g- and p-mode oscillations and are called δ Sct–γ Dor hybrids. Pressure modes probe the outer stellar layers, therefore the overall structure along the radial direction can be deduced (e.g. Kurtz et al. 2014; Saio et al. 2015).

Due to the daily aliasing and small amplitudes, the pulsations of γ Dor stars were hard to detect with ground-based observations, hence their near-core rotations were unclear for a long time. Due to the *Kepler* space telescope (Borucki et al. 2010; Koch et al. 2010), 4-yr light curves of many stars have been collected. Kurtz et al. (2014) measured the rotational splittings of the γ Dor star KIC 11145123, which was the first robust determination of the rotation of the deep core and surface of a main-sequence star. The rotational splittings of g modes in slowly pulsating B (SPB) stars were also reported (e.g. Pápics et al. 2015). For fast rotators, as in the majority of γ Dor stars, the period spacings change quasi-linearly with period and can be used to fit the near-core rotation rate (e.g. Van Reeth et al. 2016; Christophe et al. 2018). Now, splittings or period spacings of g modes from tens of γ Dor stars were found, both in single stars and binaries, whose rotation profiles are almost uniform (e.g. Keen et al. 2015; Saio et al. 2015; Triana et al. 2015; Van Reeth et al. 2015; Guo, Gies & Matson 2017; Kallinger et al. 2017 ; Li et al. 2019a, b).

In this paper, we report 960 period-spacing patterns from 611 *Kepler* γ Dor stars, which form the largest sample of identified period-spacing patterns. The period spacing ΔP is defined as the period difference between two consecutive overtones $\Delta P_n \equiv P_{n+1} - P_n$ and is a constant in the non-rotating homogeneous stars (according to the asymptotic relation, Shibahashi 1979). The rapid rotation changes stellar structure and frequency values, and the traditional approximation of rotation (TAR), or the complete calculation including the full effect of rotation is necessary to describe the oscillation frequencies more accurately (e.g. Eckart 1960; Lee & Saio 1987; Townsend 2005; Saio et al. 2018b). Under the TAR, the period spacing decreases with period quasi-linearly for the prograde and zonal g modes. Overall, the retrograde g modes have increasing period spacing (Bouabid et al. 2013; Ouazzani et al. 2017) and they are seen in slow rotators but are hard to see in fast rotators (Saio et al. 2018b; Li et al. 2019a).

In addition to g modes and sometimes p modes, γ Dor stars also show Rossby modes (r modes), whose restoring force is the Coriolis force (Papaloizou & Pringle 1978). Rossby modes propagate retrograde to the rotation direction and have discrete frequencies smaller than the rotation frequency in the corotating reference frame (Provost, Berthomieu & Rocca 1981; Saio 1982; Lee & Saio 1997). Rossby modes can also be described by the TAR and they also show a quasi-linear period-spacing pattern, in which the period spacing increases with period. Using the period-spacing patterns from g and r modes, the near-core rotation of tens of γ Dor stars were measured to be around 1 d^{-1} (e.g. Saio et al. 2018a; Van Reeth et al. 2018; Li et al. 2019b). Many of the stars in our sample also show r modes.

We describe our data reduction and TAR fitting in Section 2. Section 3 gives the observation results, including the observed relative occurrence rates of different types of modes, the typical structure of the periodogram, the slope–mean period relation of γ Dor stars. Section 4 shows the TAR fit results, including the distributions of the asymptotic spacings and the near-core rotation rates, as well as the comparison with the theoretical predictions. Section 5 reveals that the slope–period relation can be used on estimating the near-core rotation rate. Section 6 reports 11 fast-rotating stars with rotational splittings and Section 7 displays 58 stars with surface rotation modulations. Finally, we conclude our works in Section 8.

2 DATA ANALYSIS

We examined 2085 stars with effective temperature between 6000 and 10 000 K, where we used the input temperatures from the *Kepler* DR25 data release (Mathur et al. 2017). We found 960 clear period-spacing patterns in 611 stars, including 50 stars by Van Reeth et al. (2015), 22 stars with splittings by Li et al. (2019a), 82 stars with r-mode patterns by Li et al. (2019b), 30 stars by Chowdhury et al. (2018), 44 stars by Murphy et al. (2018), 344 stars found by Barbara et al. (in preparation), and the rest we found by visually inspecting light curves and their Fourier transforms (the samples overlap). Barbara et al. (in preparation) applied a Gaussian mixture model in a reduced 5D space to classify 12 066 stars in the *Kepler* field. The method involves using a greedy algorithm to select defining features from the HCTSA feature library (Fulcher, Little & Jones 2013; Fulcher & Jones 2017).

We used 4-yr *Kepler* long-cadence light curves (29.45-min sampling) from the multiscale MAP data pipeline (Stumpe et al. 2014). The 4-yr long-cadence data are suitable for γ Dor stars since the typical pulsation periods of these stars are around 1 d with period spacings around 1000 s, which require a long observation span to resolve the modes. However, 97 of our stars also have short-cadence data. These data can be used to readily investigate the pressure modes if they are γ Dor–δ Sct hybrids, though due to the super-Nyquist asteroseismology technique (Murphy, Shibahashi & Kurtz 2013) the *Kepler* LC data are also sufficient for this purpose.

In each quarter, the light curve was divided by a second-order polynomial fit to remove any slow trend. We computed the Fourier transform and extracted the frequencies until the signal-to-noise ratio (S/N) was smaller than 3.

The period-spacing patterns were identified by the cross-correlation algorithm described by Li et al. (2019a) and inspected visually. We present the period-spacing patterns of KIC 7694191 as an example in Fig. 1. Fig. 1(a) shows the periodogram, where the locations of peaks for each pattern are shown with dashed vertical lines. We found two period-spacing patterns around 0.20 and 0.38 d. The right pattern in Fig. 1(a) comprises the dipole ($l = 1$) sectoral ($m = l = 1$) g modes while the left one comprises the quadrupole ($l = 2$) sectoral ($m = l = 2$) g modes. The mode identifications were based on the TAR fit and Saio et al. (2018b), as described below.

Fig. 1(b) presents the period spacing versus period. The period spacing for the dipole g modes decreases from 400 to 100 s with increasing period. For the quadrupole g-mode pattern, the period spacing drops from 150 to 50 s with increasing period. Both patterns show deviations from the linear model, such as the dip at 0.39 d in the dipole g-mode pattern. In a rapidly rotating star, the dip is more likely to form because of the mode coupling between sectoral and tesseral modes (Saio et al. 2018b). The linear fits and their uncertainties with the dips removed are shown by the black and grey dashed lines. Hence the linear fits are not affected by the dips.

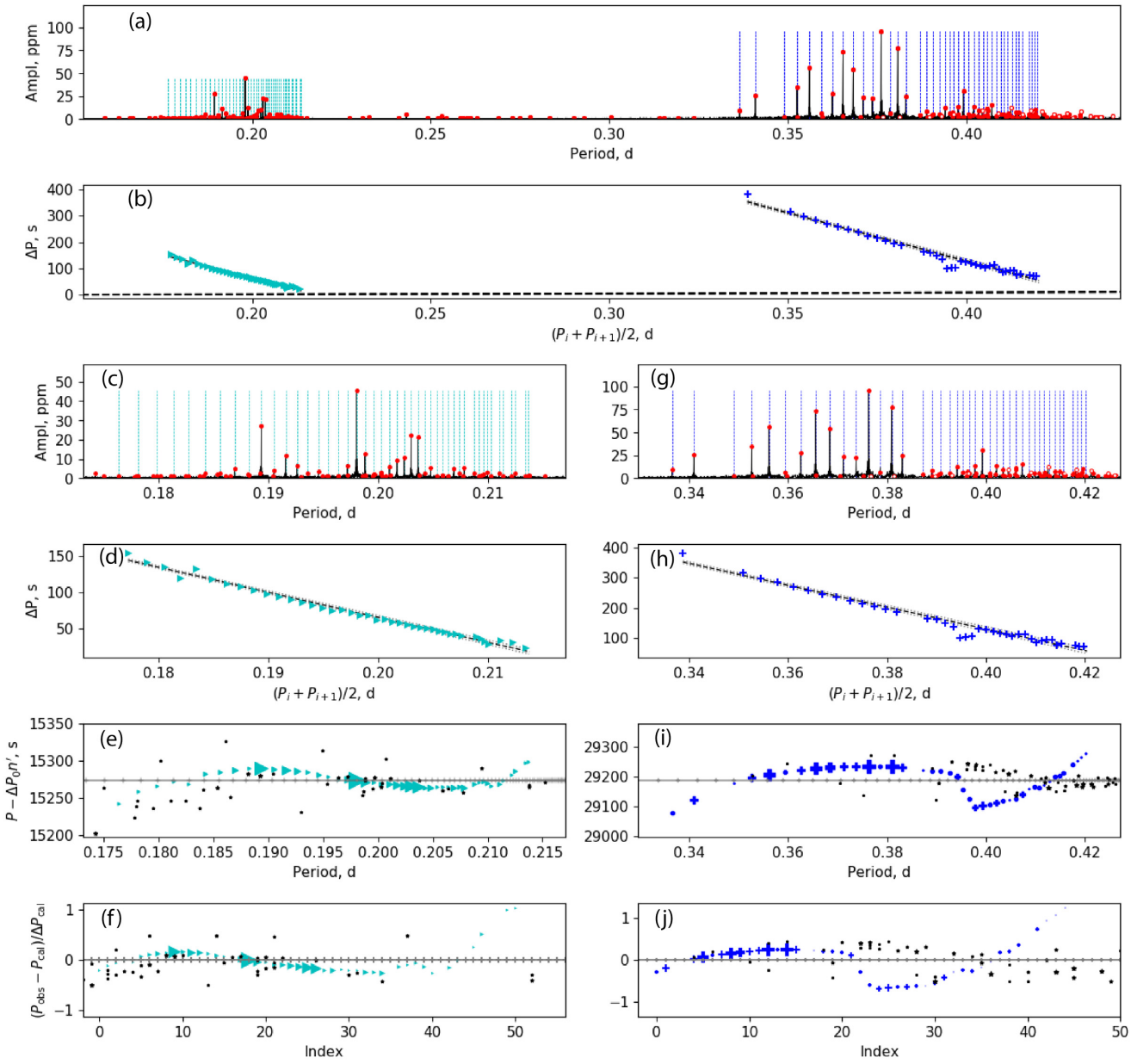

Figure 1. The g-mode patterns of KIC 7694191. Panel (a): the amplitude spectrum with x-axis of period. The y-axis is the amplitude in ppm. The solid red circles present the detected independent frequencies while the open red circles show the combination frequencies. The vertical dashed lines are the linear fits for each pattern. We found two independent frequency groups around 0.20 and 0.38 d. There are two period-spacing patterns. The blue one on the right is the $l = 1$, $m = 1$ g modes while the cyan one on the left is the $l = 2$, $m = 2$ g modes, whose periods are marked by the vertical dashed lines. Panel (b): the period-spacing patterns of KIC 7694191. The linear fits and uncertainties are shown by the black and grey dashed lines with dips removed. The blue plus symbols are the dipole g modes and the cyan triangle symbols are the quadrupole g modes. Panels (c) and (d): the detail of the spectrum and period-spacing pattern of quadrupole g modes. Panel (e): the sideways Échelle diagram of the quadrupole g-mode pattern. The cyan triangles are the periods belonging to the pattern while the black stars are the noisy peaks. Panel (f): the normalized sideways Échelle diagram of the quadrupole g-mode pattern. Panels (g)–(j): same as (c)–(f) but for the dipole g-mode patterns.

After obtaining the initial estimates for the parameters from the cross-correlation algorithm, the sideways Échelle diagram was made based on the formula

$$P_i = \Delta P_0 \frac{(1+\Sigma)^i - 1}{\Sigma} + P_0 = \Delta P_0 \left(n' + \epsilon\right), \quad (1)$$

with the assumption that the period spacing changes linearly with period. Here, P_i is the ith pulsation period, P_0 is the first pulsation period, ΔP_0 is the first period spacing, Σ is the slope in the linear assumption, $n' \equiv \frac{(1+\Sigma)^i - 1}{\Sigma}$ is the normalized index, and ϵ is the ratio $P_0/\Delta P_0$ (Li et al. 2019a). The x-axis of the sideways Échelle diagram is the observed period and the y-axis is the difference between the observed and fitted periods from equation (1).

Panels (c) and (d) zoom in on the quadrupole g modes from panels (a) and (b), while panels (g) and (h) do the same for the dipole g modes. In panels (e) and (i), the Échelle diagrams are plotted sideways. The x-axis is the pulsation period while the y-axis

is the term $P^{\rm obs} - n^{'}\Delta P$ from the fit of equation (1). During this fit, we did not exclude any dips. For the peaks that do not belong to the pattern, we plotted them at the location that minimized the value $P^{\rm obs} - n^{'}\Delta P$. Therefore, the y-axis reflects the deviation from the linear fit, similar to the curvature in the Échelle diagram of solar-like oscillators (e.g. Mazumdar et al. 2014). In panel (e), the curve is smooth and is dominated by the slightly changing slope in the quadrupole sectoral g modes. In panel (i), there is a rapid drop at 0.39 d, which is caused by the dip here. Panels (f) and (j) show the normalized sideways Échelle diagram. The x-axis is the index of peaks, counting the first peak as 0 and the y-axis is the deviation over the local period spacing $(P^{\rm obs} - n^{'}\Delta P)/\Delta P$ expressed as a percentage.

For each period-spacing pattern, consisting of a series of pulsation periods $\{P_i\}$, we measured three observables: the mean period, the mean period spacing, and the slope. The mean period $\langle P\rangle$ is the average of the pulsation periods. The mean period spacing $\langle\Delta P\rangle$ is the slope of the linear fit between the periods P_i and the index i. The slope Σ is the changing rate between the period spacing and the period with dips removed.

After identifying a period-spacing pattern, the asymptotic formulation of the TAR was used to fit the pattern assuming rigid rotation (e.g. Eckart 1960; Lee & Saio 1997; Townsend 2003a; Van Reeth et al. 2016). The pulsation periods in the corotating reference frame were computed by

$$P^{\rm TAR}_{nlm,{\rm co}} = \frac{\Pi_0}{\sqrt{\lambda_{l,m,s}}}\left(n + \varepsilon_g\right), \tag{2}$$

where Π_0 is the asymptotic period spacing, n is the radial order, the phase term ε_g is set as 0.5, and $\lambda_{l,m,s}$ is the eigenvalue of the Laplace tidal equation, which is specified by the angular degree l for g modes or the value k for r modes, the azimuthal order m, and the spin parameter s. The value k is used since the angular degree l is not defined for r modes (Lee & Saio 1997). The spin parameter is defined as

$$s \equiv \frac{2f_{\rm rot}}{f_{\rm co}}, \tag{3}$$

where $f_{\rm rot}$ is the rotation frequency and $f_{\rm co}$ is the pulsation frequency in the corotating frame. The TAR periods in the inertial reference frame are given by

$$P^{\rm TAR}_{nlm,{\rm in}} = \frac{1}{1/P^{\rm TAR}_{nlm,{\rm co}} + mf_{\rm rot}}. \tag{4}$$

Hence the near-core rotation rate, the asymptotic spacing, and the radial orders can be obtained by fitting these pulsation periods to the observed pattern using a Markov Chain Monte Carlo (MCMC) optimizing code described by Li et al. (2019b). Fig. 2 presents the TAR fitting result of KIC 7694191. The near-core rotation rate is $2.083 \pm 0.009\,{\rm d}^{-1}$ and the asymptotic spacing is 4400 ± 200 s. The best-fitting curves (dashed lines) follow the observed pattern and show slowly changing slopes with period.

3 RESULTS

The parameters of the stars, the period-spacing patterns and the TAR fit results are listed in the online only table, while Table 1 shows part of the table for guidance on style and content. We also indicate which of the 97 stars have short-cadence data and we indicated which of the 124 stars show significant pressure modes oscillations. 10 have both. These give the possibility to investigate core-to-surface physics by using g and p modes together. All the

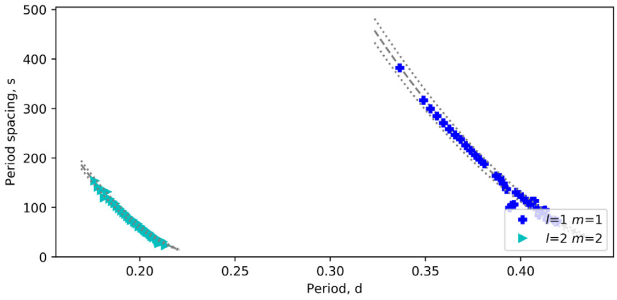

Figure 2. The TAR fitting of KIC 7694191. The dashed lines are the best-fitting result and the dotted lines show the uncertainty.

period-spacing patterns are shown in Appendix A, which is also online only.

3.1 Mode identification

The periodogram of a γ Dor star generally shows peak groups which overlap with the harmonics of fundamental frequencies. We accepted the explanation by Saio et al. (2018b) that the peak groups are prograde sectoral g-mode oscillations of increasing angular degree. Many quadrupole modes are seen in our sample. Fig. 3 shows the correlation between the mean periods of $l = 2$, $m = 2$ and $l = 1$, $m = 1$ g modes. We find that the mean periods of quadrupole sectoral g modes are typically half those of dipole sectoral g modes, since the quadrupole sectoral g modes generally coincide with the second harmonics of dipole modes.

Fig. 4 shows the slope relation between dipole and quadrupole g modes. We find that the slopes of $l = 2$, $m = 2$ g modes are similar but slightly smaller than those of $l = 1$, $m = 1$ g modes. We therefore conclude two features of the quadrupole sectoral g modes in γ Dor stars:

(i) the mean period of the quadrupole modes is half that of the dipole sectoral g modes.
(ii) the slopes of quadrupole and dipole sectoral ($l = m$) g modes are almost equal.

These features are common in most of the stars and help identify the modes. If not, several conditions should be considered: if the power spectrum is contaminated by a binary, or if they are $m = 1$ and $m = 0$ modes showing large splittings (see the example and discussion in Section 6).

We plot the periodograms of all the γ Dor stars in Fig. 5 Each row displays the normalized periodogram of one star, sorted vertically by the mean period of the dipole modes. Three ridges are seen: the dominant one is $l = 1$, $m = 1$ g modes; the ridge of $l = 2$, $m = 2$ g modes appears on the left, as these modes overlap with the second harmonics of the dipole modes; the third ridge is the $k = -2$, $m = -1$ r modes. We see that the $l = 1$, $m = 1$ g modes in γ Dor stars generally show the largest amplitudes. Assuming the dipole sectoral g modes appear around period of P, the quadrupole g modes are expected to appear around $0.5P$ and the r modes are more likely to appear around $2P$ (Li et al. 2019b). This structure of γ Dor periodograms helps guide the mode identification.

We find that four stars (KIC5876187, KIC9344493, KIC10091792, KIC10803371) show $l \geq 3$ g modes. These high-l g modes have smaller amplitudes and generally have periods below the lower boundary of our detection region (0.2–2 d), hence they

Table 1. KIC numbers, Kepler magnitudes K_p, effective temperatures T_{eff}, luminosities L, mode identifications (for g modes, we give the angular degrees l and the azimuthal orders m, while for r modes, we list the value k and m), mean pulsation periods $\langle P \rangle$, mean period spacings $\langle \Delta P \rangle$, slopes Σ, asymptotic spacings Π_0, near-core rotation rates f_{rot}, the ranges of radial orders n, and ranges of spin parameters s of 611 stars in this paper. For the last two columns, '1' marks the stars which have short-cadence data (SC) or are γ Dor–δ Sct hybrids (H).

KIC	K_p	T_{eff} (K)	L ($L_\odot$)	l	k	m	$\langle P \rangle$ (d)	$\langle \Delta P \rangle$ (s)	Σ (d/d)	Π_0 (s)	f_{rot} (d^{-1})	n (min)	n (max)	s (min)	s (max)	SC	H
1026861	11.00	7060 ± 80	8.5 ± 0.5	2		2	0.8	530	−0.0123 ± 0.0002	4310 ± 50	0.311 ± 0.002	57	92	0.7	1.3	1	
				1		1	1.5	1240	−0.0167 ± 0.0007			45	79	1.1	2.1		
1160891	13.21	6840 ± 80		1		1	0.6	200	−0.022 ± 0.002	2800 ± 400	1.14 ± 0.03	66	88	4.5	6.2		
1162345	11.68	6500 ± 200	38 ± 3	2		2	0.3	70	−0.0275 ± 0.0002	4400 ± 400	1.46 ± 0.02	55	71	3.9	5.1		
				1		1	0.5	290	−0.0372 ± 0.0003			35	47	4.8	6.6		
1295531	11.94	6760 ± 80		1		1	0.8	1280	−0.0266 ± 0.0002	4200 ± 20	0.572 ± 0.002	18	50	0.8	2.5		
1431379	12.62	6670 ± 80	8.5 ± 0.7	2		2	0.3	200	−0.0384 ± 0.0006	4360 ± 10	1.2526 ± 0.0006	21	59	1.2	3.6		
				1		1	0.6	330	−0.0349 ± 0.0005			25	66	2.9	8.1		
					−2	−1	1.0	390	0.0504 ± 0.0004			12	60	7.1	23.1		
1432149	11.22	7500 ± 300	11.6 ± 0.8	2		2	0.3	80	−0.0269 ± 0.0003	4200 ± 400	1.38 ± 0.02	54	75	3.4	4.8	1	
				1		1	0.5	260	−0.0320 ± 0.0004			44	52	5.5	6.5		
1575977	13.61	7300 ± 300	8.8 ± 0.7	1		1	0.4	710	−0.0543 ± 0.0007	3800 ± 100	1.50 ± 0.02	18	28	2.0	3.3		1
1872262	13.74	7100 ± 200	7.6 ± 0.6	2		2	0.5	260	−0.028 ± 0.002	5000 ± 2000	0.70 ± 0.05	50	58	2.0	2.4		
1996456	11.44	7100 ± 200	10.1 ± 0.8	2		2	0.4	160	−0.0294 ± 0.0002	4450 ± 80	1.038 ± 0.004	30	84	1.4	4.3	1	
				1		1	0.7	420	−0.0338 ± 0.0002			30	63	2.8	6.3		
2018685	14.05	6700 ± 200	8.4 ± 0.7	2		2	0.3	160	−0.0315 ± 0.0004	4200 ± 200	1.27 ± 0.01	32	57	1.8	3.4		
				1		1	0.6	350	−0.0343 ± 0.0005			35	50	4.1	5.9		
2020444	13.00	6890 ± 80	8.9 ± 0.7	1		1	1.0	1040	−0.0211 ± 0.0004	4360 ± 30	0.499 ± 0.002	30	66	1.2	3.1		
2141387	12.15	7200 ± 300	7.0 ± 0.6	1		1	1.0	1010	−0.035 ± 0.001	6090 ± 90	0.592 ± 0.003	29	51	2.1	4.0		
2163896	13.12	6900 ± 200	4.8 ± 0.3	1		1	0.8	460	−0.0249 ± 0.0002	3400 ± 100	0.834 ± 0.008	44	74	2.5	4.5		
2168333	10.08	8400 ± 300	34 ± 3	1		1	0.5	220	−0.0358 ± 0.0004	4200 ± 200	1.66 ± 0.01	31	62	4.5	9.5	1	1
2300165	11.05	7400 ± 300	7.2 ± 0.6	2		2	0.3	170	−0.0300 ± 0.0002	4140 ± 70	1.136 ± 0.004	29	75	1.4	3.9	1	
				1		1	0.6	380	−0.0323 ± 0.0003			26	71	2.4	7.4		
2309579	13.35	7200 ± 300	10.0 ± 0.7	2		2	0.4	110	−0.0211 ± 0.0002	4000 ± 200	1.001 ± 0.007	58	95	2.5	4.2		
				1		1	0.8	210	−0.0230 ± 0.0001			50	107	4.3	9.4		
2449383	13.92	7200 ± 300	7.6 ± 0.6	2		2	0.2	90	−0.0310 ± 0.0003	3910 ± 90	1.588 ± 0.007	35	76	2.3	5.2		
				1		1	0.4	320	−0.0419 ± 0.0004			20	59	2.5	8.0		
2450944	15.74	6800 ± 200		1		1	1.0	2500	−0.0084 ± 0.0004	4136 ± 5	0.141 ± 0.001	24	37	0.2	0.3		1
				1		−1	1.2	3350	0.003 ± 0.001			30	37	0.2	0.3		
2575161	10.88	6900 ± 100		1		1	0.4	250	−0.0466 ± 0.0008	4470 ± 20	1.833 ± 0.001	20	54	3.6	10.0		
					−2	−1	0.7	580	0.0753 ± 0.0004			8	27	7.3	16.2		
2578582	13.93	7300 ± 300	5.2 ± 0.4	1		1	0.8	1140	−0.0233 ± 0.0003	3960 ± 30	0.570 ± 0.003	24	53	1.0	2.5		
2579147	13.83	7300 ± 300	14 ± 1	2		2	0.7	620	−0.0096 ± 0.0004	3600 ± 30	0.286 ± 0.003	54	72	0.5	0.7		1
				1		1	1.1	1560	−0.0154 ± 0.0006			43	51	0.8	0.9		
2696217	13.45	7400 ± 300	7.0 ± 0.5	1		1	1.3	1310	−0.0130 ± 0.0002	3460 ± 20	0.290 ± 0.001	39	84	0.7	1.7		
2710406	13.27	6960 ± 80	12.6 ± 0.9	1		1	1.5	2270	−0.0054 ± 0.0003	4270 ± 70	0.138 ± 0.006	45	57	0.4	0.6		
2710594	11.79	7200 ± 200	8.0 ± 0.5	1		1	0.7	360	−0.0290 ± 0.0003	4000 ± 10	0.9920 ± 0.0006	27	86	2.3	7.9		
					−2	−1	1.2	470	0.0381 ± 0.0005			20	64	7.4	18.0		
2719928	12.66	7200 ± 200	9.6 ± 0.7	2		2	0.3	70	−0.0275 ± 0.0004	3700 ± 700	1.47 ± 0.04	55	82	3.3	5.0		
				1		1	0.5	150	−0.006 ± 0.004			59	69	7.1	8.4		
2846358	11.02	6800 ± 200		2		2	0.4	360	−0.0279 ± 0.0004	4020 ± 50	0.755 ± 0.004	25	61	0.7	2.0	1	
				1		1	0.8	650	−0.0336 ± 0.0004			32	63	1.9	4.0		

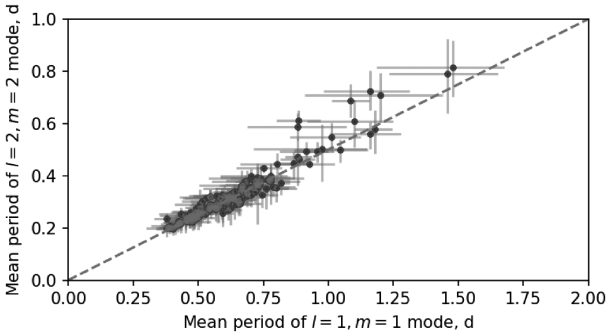

Figure 3. The observed period relation between $l = 2$, $m = 2$ and $l = 1$, $m = 1$ g modes. The error bars show the pulsation period spans, not the uncertainties. The dashed line shows the relation that the mean period of $l = 2$, $m = 2$ g modes is half that of $l = 1$, $m = 1$ g modes.

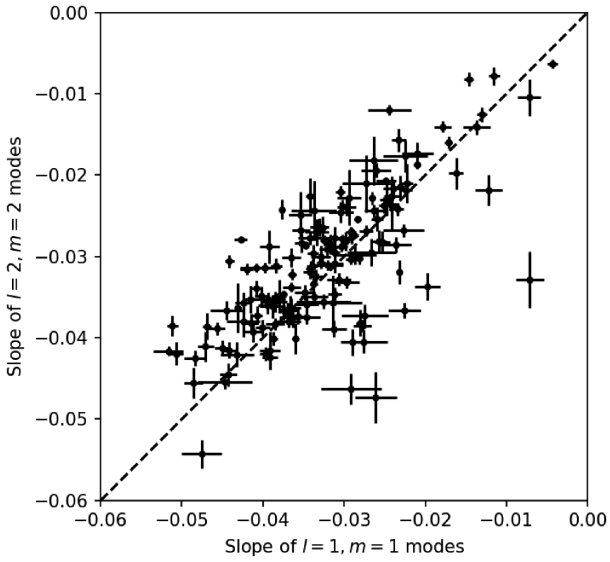

Figure 4. The slope relation between the observed $l = 2$, $m = 2$ and $l = 1$, $m = 1$ g modes. We only plot the points with slope error smaller than 0.005. The dashed line shows the place where the slopes are equal.

are hard to detect. However, for dipole and quadrupole g modes, we confirm that the results listed in Table 1 are complete.

3.2 Occurrence rate of modes

Fig. 6 shows the observed relative occurrence rates of different modes. Among all the 960 patterns, 62.0 per cent are $l = 1$, $m = 1$ g modes. The second most common modes are $l = 2$, $m = 2$ g modes, which constitute 18.9 per cent of the total detection. Rossby modes are the third most common modes (11.5 per cent). Apart from these three modes, we also see $l = 1$, $m = 0$ and $l = 1$, $m = -1$ modes with percentages of 3.0 per cent and 2.3 per cent, respectively, which were mainly found in the slow rotators reported by Li et al. (2019a). 11 fast rotators with splittings are detected in this work, which will be described in Section 6.

There are a few patterns that cannot be classified into those five types of modes above. They might be the sectoral g modes with higher angular degree ($l = 3$, $m = 3$ for example, see KIC 9344493), or the only $k = -1$, $m = -1$ r mode reported by Li et al. (2019b),

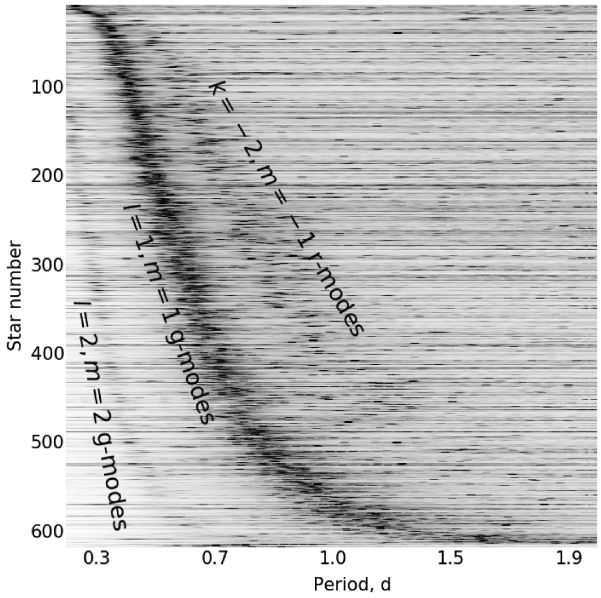

Figure 5. The periodograms of all the γ Dor stars with identified period-spacing patterns in our sample. Each row shows the periodogram for one star. The colour stands for the normalized amplitudes to the power of 0.25 for the best visibility. The trends of $l = 1$, $m = 1$ g modes, $l = 2$, $m = 2$ g modes, and $k = -2$, $m = -1$ r modes are seen and marked by the texts.

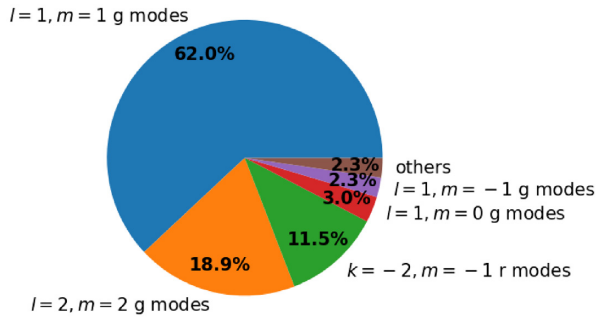

Figure 6. The percentages of different oscillation modes among 960 patterns.

or $l = 2$, $m = 1$ g modes in two newly discovered fast rotators (KIC 5092681 and KIC 5544996), or some patterns that cannot be fitted with the TAR. All of these occupy 2.3 per cent of the total detected period-spacing patterns.

Fig. 7 shows the numbers of stars which show different oscillation modes. We classify the modes into three main types: $l = 1$ g modes, $l = 2$ g modes, and $k = -2$, $m = -1$ r modes. There are 339 stars that only show $l = 1$ g modes (red area) and 145 stars that show both $l = 1$ and $l = 2$ g modes (yellow area). Almost all the stars have $l = 1$ g-mode period-spacing patterns. However, there are power excesses over $l = 1$ g-mode regions in 16 stars without period-spacing patterns identified. For these stars only $l = 2$ g-mode patterns are reported. We notice that KIC 5491390 is the only star that does not show any $l = 1$ g-mode power excess. In total, there are 17 stars with only $l = 2$ g modes (green area). Zhang et al. (2018) reported that KIC 10486425 also oscillates only in $l = 2$ g modes. The reason for the absence of $l = 1$ g modes needs further investigation.

We do not find any star that only shows r modes. The reason is that the TAR cannot converge well if g-mode patterns are absent,

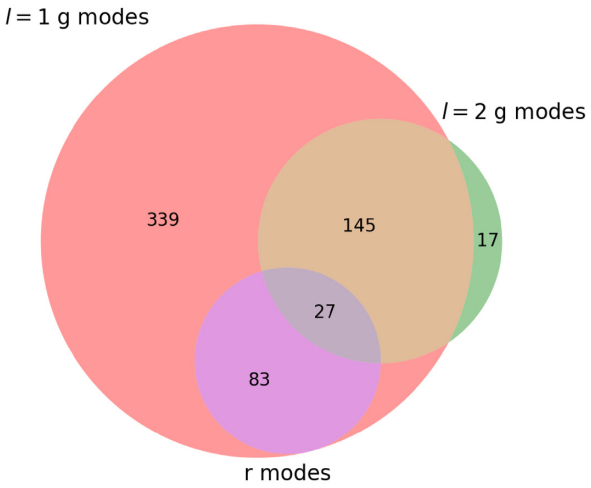

Figure 7. The numbers of stars with observed period-spacing patterns.

hence we cannot ensure that the observed pattern is a real r-mode pattern, or we are misled by missing peaks in the observed pulsation spectra. Hence, all the r modes co-exist with g modes in our sample. There are 83 stars with $l = 1$ g modes and r modes, and there are 27 stars with $l = 1$, $l = 2$ g modes, and r modes. The co-existence of g mode and r modes decreases the uncertainties of near-core rotation rates significantly. The typical uncertainty is 0.0009 d^{-1} for the stars with both g and r modes, while it is 0.008 d^{-1} for the stars with only g modes.

3.3 Slope–period diagram

In Section 2, we introduced three observables for each pattern, the mean period, the mean period spacing, and the slope. Fig. 8 shows the relation between the slopes and the mean periods from all the patterns in our sample, hence we call this diagram the Slope–Period (S–P) diagram. The mean period and the slope are correlated. We find that the data points of $l = 1$, $m = 1$ g modes, $l = 2$, $m = 2$ g modes, slowly rotating g modes, and $k = -2$, $m = -1$ r modes form four different groups which have diverse trends and clear boundaries.

(i) $l = 1$, $m = 1$ g modes: these points are the majority, which are shown by the blue triangles. Most patterns have mean periods between 0.4 and 0.8 d and slopes around ~ -0.04. They show a positive correlation between the slopes and the mean periods.

(ii) $l = 2$, $m = 2$ g modes: those points are presented by the green stars. These modes have shorter periods than dipole modes (between 0.2 and 0.4 d) but have similar slopes (~ -0.04) as pointed out in Section 3.1.

(iii) $l = 1$, $m = 0$ and $l = 1$, $m = -1$ g modes: they are marked by the yellow circles and the red rectangles. These two modes are rare (for $m = 0$) or absent (for $m = -1$) in rapid rotators but are seen in the slow rotators reported by Li et al. (2019a). Due to the slow rotation rate, the rotational effect is not strong so the period spacings in those modes remain nearly identical. Hence we see most $m = 0$ and $m = -1$ modes around the horizontal line with slope of zero.

(iv) $k = -2$, $m = -1$ r modes: they are the red circles. As discussed by Li et al. (2019b), r modes have positive slopes and show an inverse correlation between the mean period and the slope.

Fig. 8 displays the typical locations of different modes on the S–P diagram. It can be used for mode identification. When a new pattern is found, its location on the S–P diagram reveals its mode identification. If the point is an outlier, several possibilities should be considered: the period spacings are misidentified since some peaks in the amplitude spectra are too weak to be detected; the slope is strongly affected by the partially observed dips caused by chemical composition gradients (e.g. KIC 4919344 in Li et al. 2019a); or the star is an SPB star, which has a larger asymptotic spacing (Π_0) because it has a higher mass than a γ Dor star (e.g. Pápics et al. 2017). Consequently, a pattern of an SPB star has a steeper slope than a pattern of a γ Dor star with a similar mean period.

4 ASYMPTOTIC SPACING AND ROTATION

We used the TAR to fit the period-spacing patterns and measured the near-core rotation rates $f_{\rm rot}$, the asymptotic spacings Π_0 (also called buoyancy radii), and the radial orders n.

4.1 Distribution of Π_0

Fig. 9 gives the observed distributions of the asymptotic spacing Π_0. The stars show a symmetric distribution centred around $\Pi_0 = 4000$ s. We find that 68 per cent of stars have Π_0 between 3700 and 4800 s. Stars with large Π_0 are likely to be SPB stars (with Π_0 from 5600 to 16000 s; Pápics et al. 2017). They show g-mode patterns with larger period-spacing values and steeper slopes than γ Dor stars but the pulsation periods are similar. However, the effective temperatures of those possible SPB stars are located in the typical ranges of A- and F-type stars. This may indicate that the effective temperatures are wrong, or there are pulsation periods missing in the detected patterns, or the stars are very young. The stars with $\Pi_0 \lesssim 3000$ s are probably close to the terminal age main sequence.

Van Reeth et al. (2016) reported the theoretical distribution of Π_0, which was calculated based on a grid of theoretical stellar models that includes the γ Dor instability strip. The relative duration of the different evolutionary stages was also considered in the calculation. It shows that the most likely value of Π_0 is 4400 s, which is higher than the observed one. The theoretical histogram also has a slightly asymmetric shape. The discrepancy between the observed and theoretical distributions are probably caused by the different parameters, such as metallicity and mixing length, and it also reveals that a full non-adiabatic computation of the γ Dor instability strip is needed for the theoretical distribution of Π_0.

Fig. 10 shows the S–P diagram coloured by their asymptotic spacings Π_0. We found that the yellow outliers on the lower right are composed of the stars with large Π_0. They generally show steeper period-spacing patterns, hence they appear below the typical $l = 1$, $m = 1$ g-mode group of γ Dor stars. From now, we only present the results using stars with $\Pi_0 < 6000$ s to avoid any contamination from SPB stars or wrong identifications.

We show our theoretical evolutionary tracks in Fig. 11. MESA v10108 was used to compute the evolutionary tracks (Paxton et al. 2011, 2013, 2015, 2018). The tracks shown in Fig. 11 have: stellar masses are from 1.0 to 3.0 $M_\odot$ with step of 0.05 $M_\odot$, a hydrogen mass fraction X of 0.71, a metallicity Z of 0.014, a mixing length α of 1.8, an exponential core overshooting $f_{\rm ov}$ of 0.015, and an extra diffusive mixing $D_{\rm mix}$ of 1 $cm^2\,s^{-1}$, we also used the OPAL capacities and the Asplund et al. (2009) solar abundance mixture. For each stellar model, the asymptotic spacing Π_0 is calculated and the point is coloured by the observed probability density of Π_0 from Fig. 9. Two solid black lines in Fig. 11 display the boundaries of

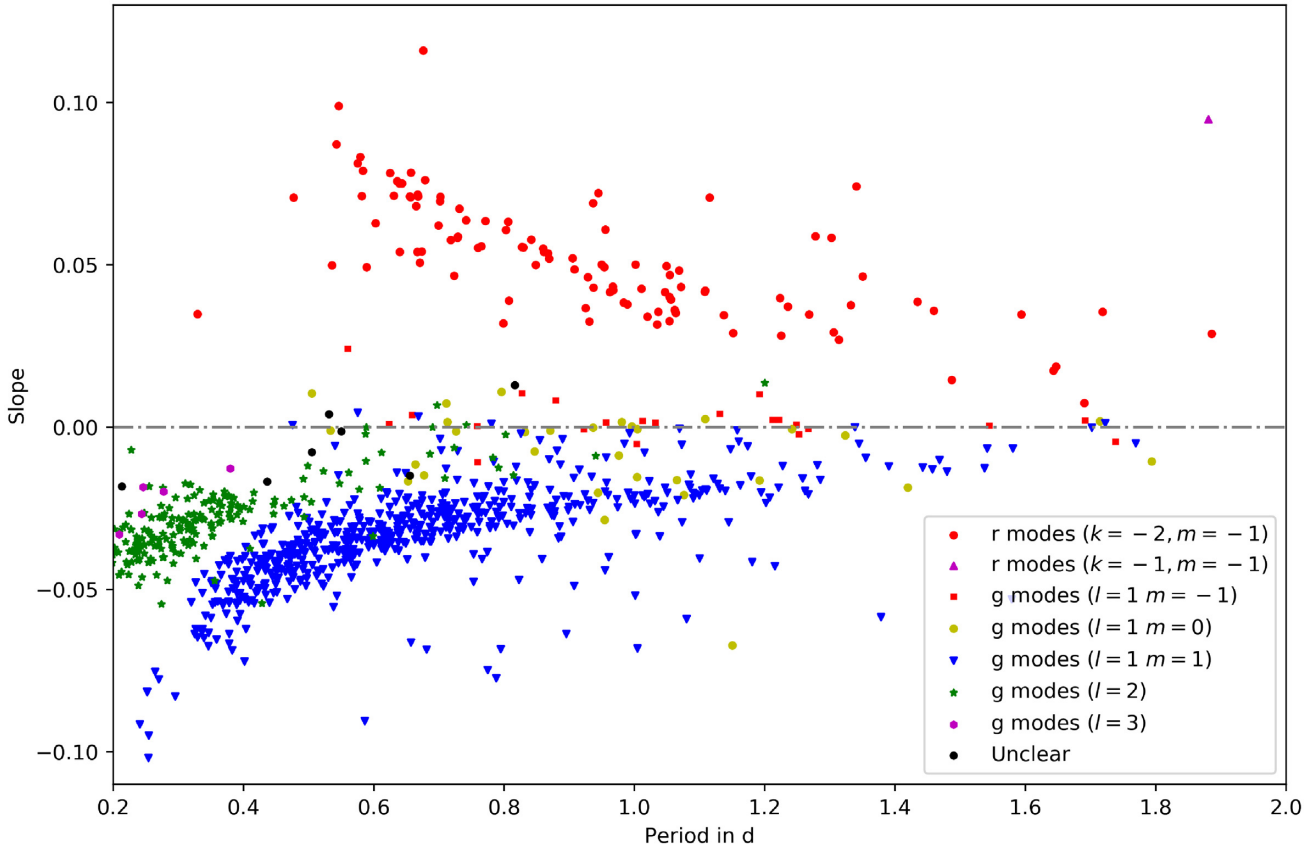

Figure 8. Slopes versus the means of the periods of 960 period-spacing patterns from 611 γ Dor stars. The x-axis is the mean period in each pattern. The y-axis is the slope between the period spacing and the period with dips removed. Different colours and symbols show different modes.

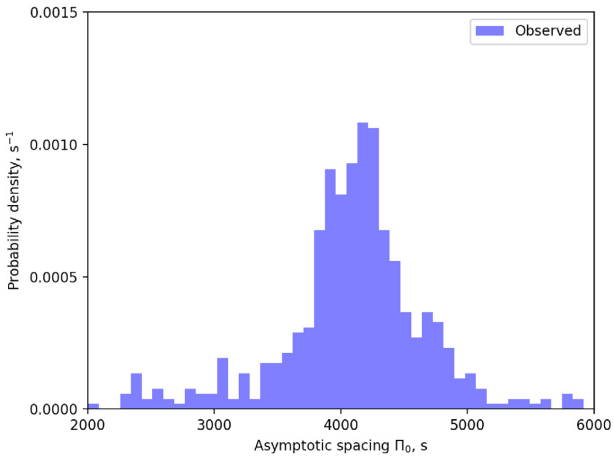

Figure 9. The observed distribution of asymptotic spacing Π_0.

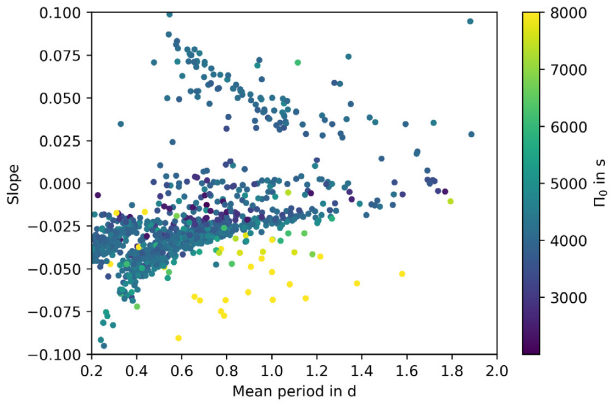

Figure 10. The S–P diagram coloured by the asymptotic spacing Π_0. The outliers on the lower right is composed of the stars with large Π_0.

the theoretical instability strip of γ Dor stars (Dupret et al. 2005). We find that the areas with high-Π_0 densities show a nearly vertical strip, broad at the zero-age main sequence (ZAMS) and narrow at the terminal-age main sequence (TAMS). The low-mass stars are more likely to pulsate near the ZAMS, while for the high-mass stars, the pulsation may happen close to the TAMS and for a shorter duration than for low-mass stars. The high-density area of Π_0 on the Hertzsprung-Russell (HR) diagram is generally consistent with the theoretical instability strip.

Combining the effective temperatures from *Kepler* DR25 (Mathur et al. 2017) and the luminosities from Murphy et al. (2019) using *Gaia* DR2 parallax (Gaia Collaboration 2016), we place our stars on the HR diagram, as shown in Fig. 12. Fig. 12 displays that most γ Dor stars are located on the lower right area, with lower effective temperature and luminosity than δ Sct stars. The low-temperature boundary of our γ Dor sample follows the theoretical instability strip (solid black lines). This may prove that the theory predicted the red boundary correctly. However, many γ Dor stars are located beyond the blue boundary of the instability strip. This could be caused by systematic offsets in the photometric $T_{\rm eff}$ values.

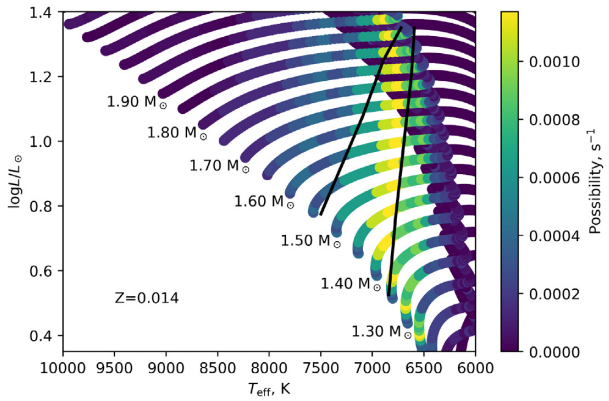

Figure 11. The probability density of Π_0 on the HR diagram. The colour stands for the probability density of Π_0 from Fig. 9. The black lines show the theoretical instability strip of γ Dor stars (Dupret et al. 2005).

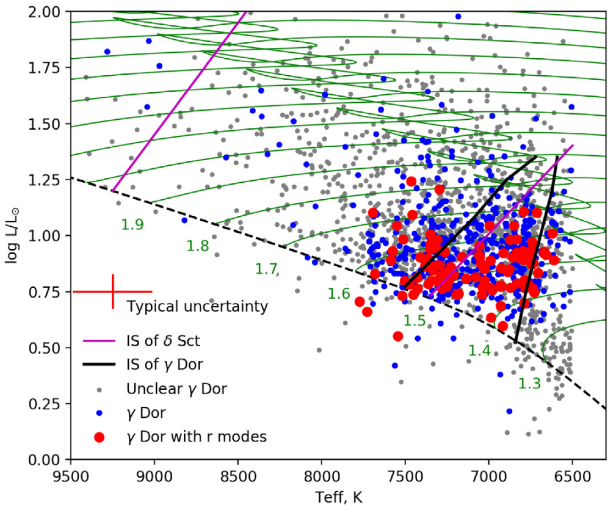

Figure 12. Stars on the HR diagram. The blue points are the γ Dor stars with clear g-mode patterns. The red points are the stars with both g- and r-mode patterns. The grey points are the stars we inspected but do not show clear period-spacing patterns. The black lines show the theoretical instability strip (IS) of γ Dor star while the purple lines depict the observed IS of δ Sct star by Murphy et al. (2019).

Typical uncertainties on these values are on the order of 250 K. More accurate $T_{\rm eff}$ values from high-resolution spectroscopy are needed to evaluate this possibility. If the $T_{\rm eff}$ values are found to be accurate, the presence of hot γ Dor stars could reflect the limit of the current theory, which was mentioned by Dupret et al. (2005). For example, a proper mixing length should be used in these stars rather than the solar value.

As mentioned before, we inspected 2085 stars and found 611 stars with clear period-spacing patterns. The grey circles in Fig. 12 are the stars without identified period-spacing patterns. They may be the γ Dor stars with unresolved g-mode patterns, or the phase-modulation binaries from Murphy et al. (2018). We included the phase-modulation binaries since they show similar $T_{\rm eff}$, but they may not necessarily be γ Dor stars. We do not find any special distributions of the stars without pulsation patterns on the HR diagram. There is no explanation about why some γ Dor stars do not show any clear period-spacing pattern. The reasons might be:

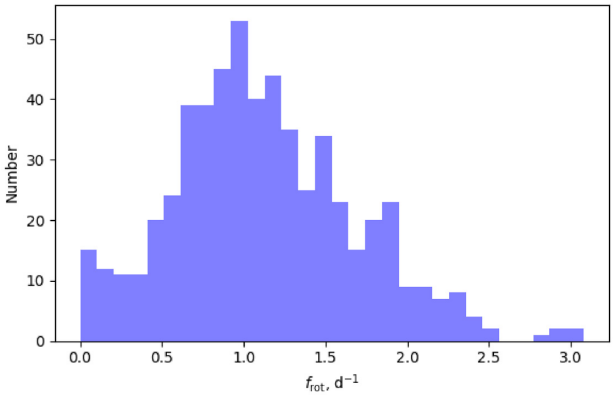

Figure 13. The distribution of observed near-core rotation rate $f_{\rm rot}$. Many stars rotate around $1\,{\rm d}^{-1}$ while there is a slow-rotator excess slower than $0.4\,{\rm d}^{-1}$, suggesting two classes of γ Dor stars.

dense, overlapping patterns that would be hard to disentangle; there are only a few excited modes, hence the pattern is incomplete.

4.2 Distribution of $f_{\rm rot}$ with slow-rotator excess

Fig. 13 displays the distribution of the near-core rotation rates $f_{\rm rot}$. Most stars have rotation frequencies around $1\,{\rm d}^{-1}$. The distribution increases rapidly after $0.4\,{\rm d}^{-1}$ and drops slowly after $\sim 1\,{\rm d}^{-1}$. The most rapid rotators are KIC 8458690A and KIC 8458690B with $f_{\rm rot} \sim 3.01\,{\rm d}^{-1}$, whose two identical period-spacing patterns form 'splittings' reported by Li et al. (2019a). However, many stars rotate less quickly than expected, which forms an excess at $f_{\rm rot} \lesssim 0.4\,{\rm d}^{-1}$ in Fig. 13.

The histogram of the near-core rotation rate in Fig. 13 shows a slow-rotator excess. We suggest defining two classes of γ Dor stars by their near-core rotation rates: (1) slow rotators with $f_{\rm rot} \lesssim 0.4\,{\rm d}^{-1}$; (2) fast rotators with $f_{\rm rot} \gtrsim 0.4\,{\rm d}^{-1}$. A similar distribution has been realized for A- and F-type stars by observing the projected velocity $v \sin i$ (e.g. Ramella et al. 1989; Abt & Morrell 1995; Royer et al. 2007). Abt & Morrell (1995) found that all the rapid rotators have normal spectra and nearly all slow rotators have abnormal spectra (Ap or Am). The extremely slow rotation rate may be explained by magnetic braking for Ap stars or tidal braking for Am stars. However, after removing Ap and Am stars, Royer et al. (2007) still found the bimodality. The slow rotators have $v \sin i < 70\,{\rm km\,s}^{-1}$ and the fast rotators have $v \sin i \sim 160\,{\rm km\,s}^{-1}$, whose ratio is consistent with our near-core rotation rate (0.4 and $1.0\,{\rm d}^{-1}$). Due to the large sample size here, the effect of inclination should be averaged out, hence we compare $v \sin i$ with our inclination-independent near-core rotation rate in the last sentence directly. Rotational braking during the main sequence can be explained in many ways, such as magnetic fields, binarity, interaction with stellar disc, or the formation of blue stragglers (e.g. Mestel 1968; Hut 1981; Takada-Hidai et al. 2017). Our sample contains a large number of slow rotators. Follow-up spectroscopic observations can obtain the chemical abundances and the surface rotations, hence we can infer the formation of the slow rotators.

According to Ouazzani et al. (2017), the slope $\Sigma = {\rm d}\Delta P/{\rm d}P$ was defined as a diagnostic for rotation. The slope decreases from zero with increasing rotation for $m \geq 0$ g modes and vice versa for the r-mode pattern. We plot the relation between the fitted near-core rotation rate and the observed slope in Fig. 14. The points clustered into two groups, corresponding to $l = 1$, $m - 1$ g modes

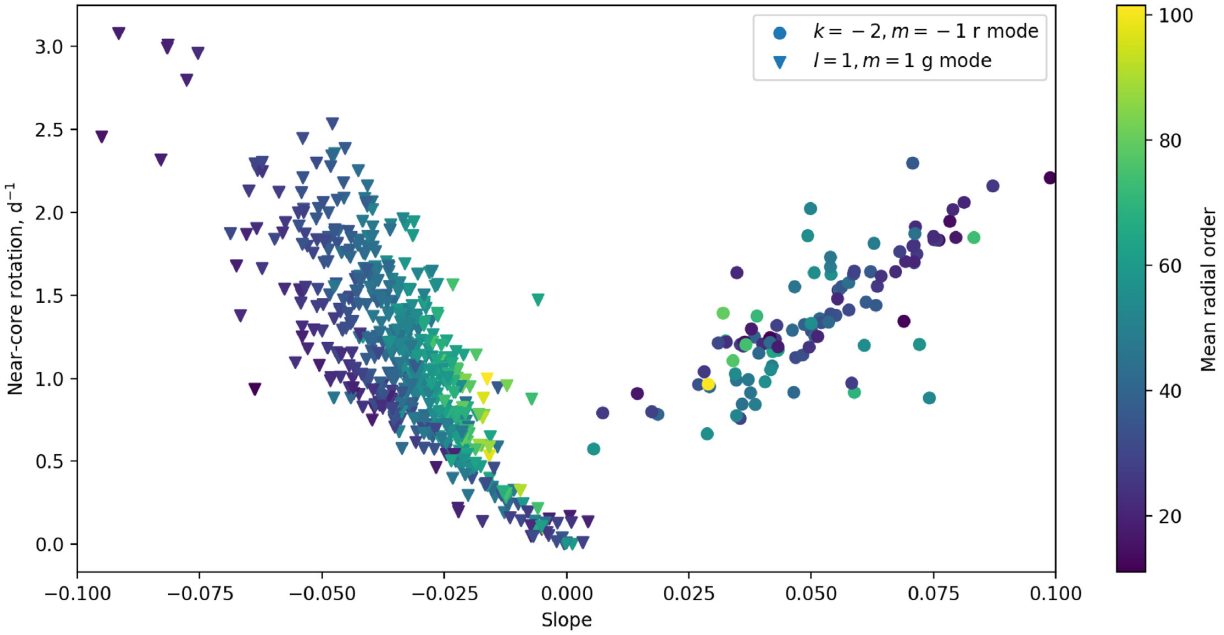

Figure 14. The relation between slope and near-core rotation rate $f_{\rm rot}$. The triangles are the $l = 1$, $m = 1$ g-mode patterns, whose slopes are generally smaller than zero hence are located on the left. The circles are the $k = -2$, $m = -1$ r-mode patterns with positive slopes on the right. The g-mode slopes are correlated with their mean radial orders, as shown by the colour gradient.

and $k = -2$, $m = -1$ r modes. For the g-mode patterns, only several slow rotators show g-mode slopes slightly larger than 0 and most points have negative slopes and are located on the left side of Fig. 14. We find the rotation–slope relation of the g modes has a large scatter ($\sigma = 0.35\,{\rm d}^{-1}$) and shows an obvious gradient with the mean radial orders. The gradient reveals that the slope for a period-spacing pattern is not only affected by the rotations and dips, but also affected by the radial orders. For a given rotation rate (for example $1\,{\rm d}^{-1}$), the slopes are generally flatter (Σ near zero) for higher radial orders. The effect of radial orders is clear and can be used to explain the widths of the trends in Fig. 8. Further discussion about the radial orders on the S–P diagram will be given in Section 5 and Fig. 21.

For the r modes, the rotation rate has a positive correlation with the slope. There is less scatter among the r-mode points ($\sigma = 0.24\,{\rm d}^{-1}$), presumably because they show a smaller spread in radial orders, as we investigate in Section 4.4. The theoretical relation between slope and near-core rotation rate also depends on the stellar parameters (such as $T_{\rm eff}$, [Fe/H]), which should be considered when comparing with observations.

Bouabid et al. (2013) predicted the relation between the pulsation period in the corotating frame versus the effective temperature, shown as the solid lines in Fig. 15. It predicted that γ Dor stars pulsate between 0.5 and 5 d in the corotating frame with effective temperature from 6600 to 7400 K. The area is triangular, implying that the long-period stars are more likely to have lower temperatures. We count the number of the $l = 1$, $m = 1$ g modes and compare our observations with the theoretical prediction in Fig. 15. The pulsation period in the inertial frame is converted into the corotating frame using the near-core rotation rate derived by the TAR fit. It shows that the corotating periods are generally between 1 and 4 d, following the theoretical prediction. However, many stars have higher photometric temperatures than the theory, which is similar to what the H–R diagram shows in Fig. 12. The peak of the observed contour is located outside the theoretical area and the pulsation period does not show any relation with effective temperature.

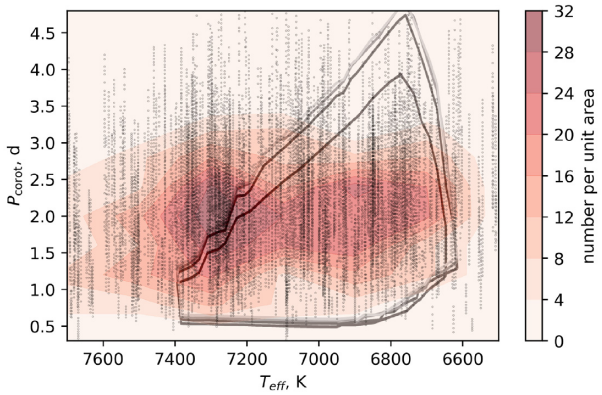

Figure 15. Pulsation period in the corotating frame versus effective temperature. One star has one effective temperature but many pulsation modes, hence the data points (black dots) show vertical fringes. The contour displays the number of the observed pulsation modes. The solid lines show the theoretical areas reported by Bouabid et al. (2013), with equatorial rotation velocities $v_{\rm eq} = 0$ (black), 30 (dark grey), 60 (grey), and 90 km s^{-1} (light grey).

4.3 Correlation between Π_0 and $f_{\rm rot}$

Fig. 16 shows the correlation between the near-core rotation rate and the asymptotic spacing. The uncertainty on Π_0 is sometimes large, due to short patterns, or when only $l = 2$, $m = 2$ g modes are seen. Hence, we only plot the 578 stars with Π_0 uncertainty within ± 500 s. The asymptotic spacing decreases with stellar evolution so it is considered an indicator of the stellar age (e.g. Saio et al. 2015; Ouazzani et al. 2018). However, the relation between Π_0 and age is affected by many other issues, for example, the shape of the

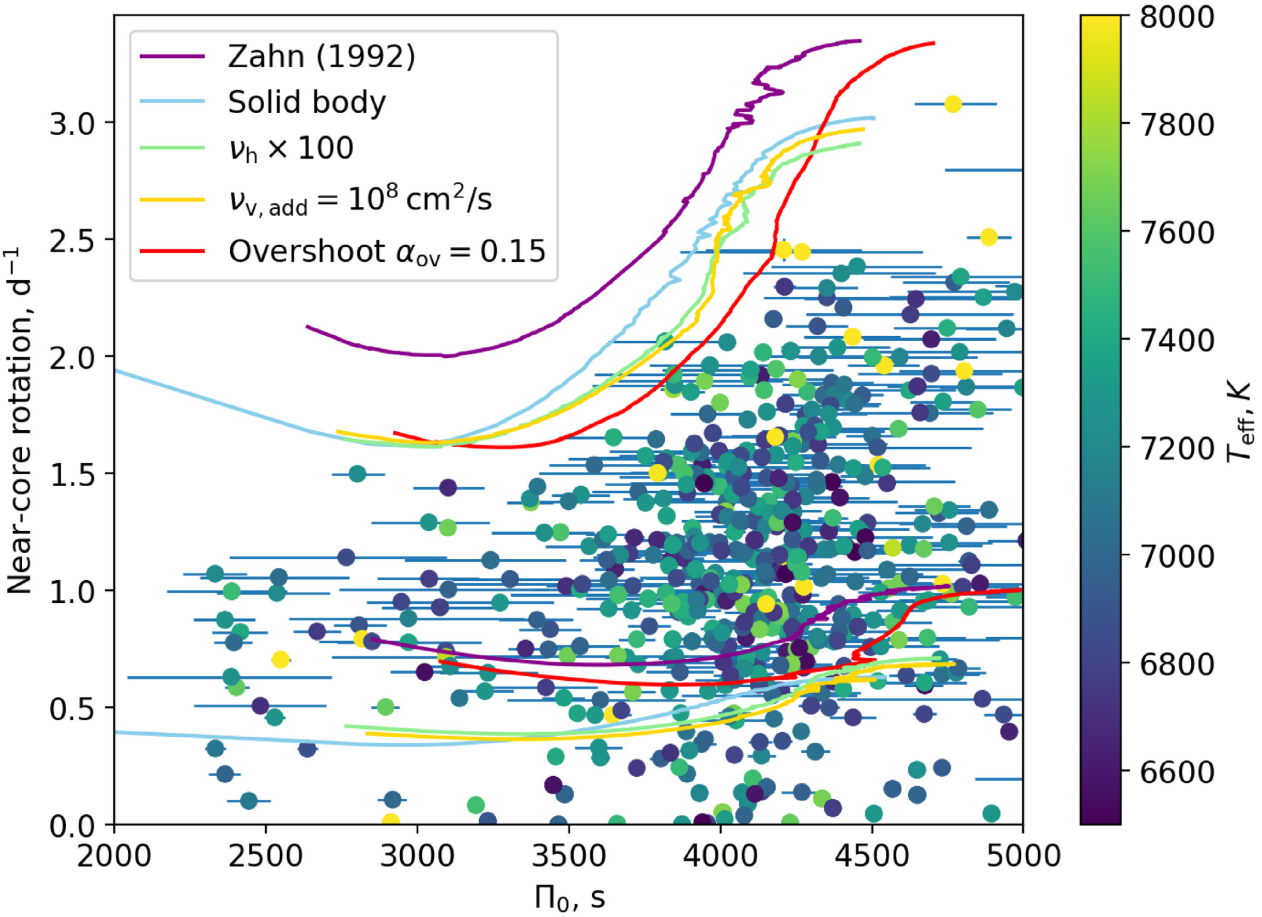

Figure 16. The correlation between asymptotic spacing Π_0 and the near-core rotation rate f_{rot}. With stellar evolution, the star moves from right to left. We only plot the points with Π_0 uncertainty smaller than 500 s. The colour stands for the effective temperature. The theoretical predictions (solid lines) are made by Zahn (1992) and Ouazzani et al. (2018), where ν_h means the enhanced horizontal viscosity, $\nu_{v,add}$ means the additional vertical viscosity.

instability strip (Fig. 11) or the initial mass. A detailed relation was reported by Mombarg et al. (2019). With stellar evolution, angular momentum is transferred and the near-core rotation also decreases. Hence, in Fig. 16, the stars evolve from upper right to lower left.

The solid lines show the theoretical boundaries calculated by the angular momentum transfer model of Zahn (1992), which considered the effects of meridional circulation and shear-induced turbulence and were calibrated by the observations of three clusters (Ouazzani et al. 2018). We plot the theoretical boundaries with different conditions, such as the original model by Zahn (1992) (purple lines), the model assuming stars are solid bodies (blue lines), the Zahn (1992) model with enhanced horizontal viscosity $\nu_h \times 100$ (green lines), or with additional vertical viscosity $\nu_{v,add}$ (yellow lines), or with overshooting $\alpha_{ov} = 0.15$ (red lines) (see details in Ouazzani et al. 2018).

Our observational points are generally located between the theoretical lines. The upper boundaries of the models from Ouazzani et al. (2018) fit the observations very well, which were calibrated by three clusters to include 80 per cent of the stars. Our observations do not have any star above these upper boundaries, implying that there is a lack of fast rotators. We also notice that there are still many slow rotators below the lower boundaries of these models, confirming the 'slow rotator accumulation' by Ouazzani et al. (2018). Our results are consistent with and expand upon the results from 37 stars by Ouazzani et al. (2018) (these stars are also in our sample).

The difference between the observations and the theory demands an explanation. Either there is a selection effect in the observations or there are ingredients missing from the stellar models that produce the theoretical predictions. We consider the former, first.

The 'fast rotators desert' might be expected if the period-spacing patterns of rapid rotators cannot be extracted from (evolved) stars with small asymptotic spacings, as is indeed the case. In other words, although patterns are extractable for $\Pi_0 = 5000$ s and $f_{rot} = 2.5$ d^{-1}, they are not extractable for $\Pi_0 = 3000$ s at the same f_{rot} due to a denser power spectrum. However, the shape of the theoretical regions in Fig. 16 matches the observational distribution and is only shifted from it. Stars are not predicted at $\Pi_0 = 3000$ s and $f_{rot} = 2.5$ d^{-1}, so the 'fast rotators desert' is not the result of an observational selection effect.

What ingredients might be missing from the models that would move the theoretical region towards the observed one? One possible answer is the rigid rotation. As pointed out by Van Reeth et al. (2018) and Li et al. (2019b) and discussed in Section 7, the γ Dor stars have almost the same rotation rates between near-core and surface regions, implying a very effective mechanism of angular momentum transfer. The model with solid body condition (light blue lines in Fig. 16) indeed shifts down and is a better match to the observations. Ouazzani et al. (2018) also modified different coefficients beyond

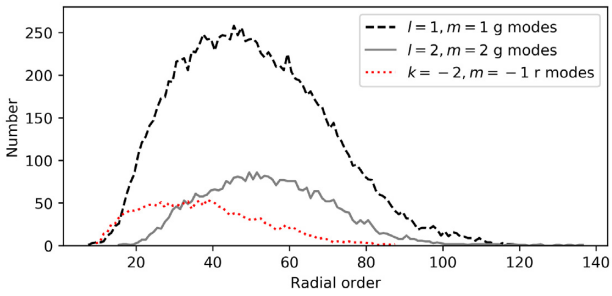

Figure 17. The distributions of radial orders of different modes.

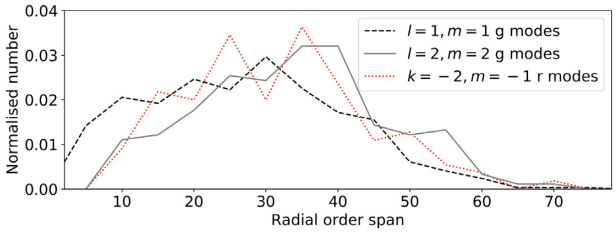

Figure 18. The normalized distributions of the pattern lengths.

their ordinary range to investigate the effect of the models, such as enhancing horizontal viscosity in the star by a factor 100, which also have the desired effects. Another governing variable is the asymptotic spacings (or called 'buoyancy radius' in Ouazzani et al. 2018); increasing the asymptotic spacings moves the theoretical region down in Fig. 16. An additional parameter that modifies the asymptotic spacings is convective overshooting above the core. Including this parameter is physically motivated, it migrates the theoretical boundaries in the direction of the observations, and may fully resolve the difference between the theory and observations, as what we see in Fig. 16.

4.4 Distributions of radial orders

Fig. 17 depicts the distributions of the radial orders for different modes, which are obtained by the best-fitting results of the TAR. We find that the distributions of the radial orders are similar to the results by Li et al. (2019b). For $l = 1$, $m = 1$ g modes, the median of the distribution is 48, and 68 per cent of modes have radial orders between 30 and 70. For $l = 2$, $m = 2$ g modes, the peak of the distribution has a slightly higher radial order than dipole g modes, and 68 per cent of modes satisfy $37 < n < 71$. We notice that the radial orders are higher than the theoretical prediction by Bouabid et al. (2013), which found that the modes with radial orders from 15 to 38 are unstable.

For $k = -2$, $m = -1$ r modes, the radial orders are generally lower than those of g modes. The median is 36, and $21 < n < 53$ is the range for 68 per cent of the modes. The distribution of r-mode radial orders is asymmetric while the distributions of g modes are almost symmetric.

Fig. 18 presents the pattern lengths for different modes. The pattern length is the difference between the maximum and minimum of the radial orders. The numbers are normalized for a clear comparison. We find that the lengths for dipole g modes, quadrupole g modes, and r modes do not show any dramatic differences. The medians are about 30 and most of them have pattern lengths between 10 and 50 radial orders. Several patterns are extremely long, even up to 70 radial orders.

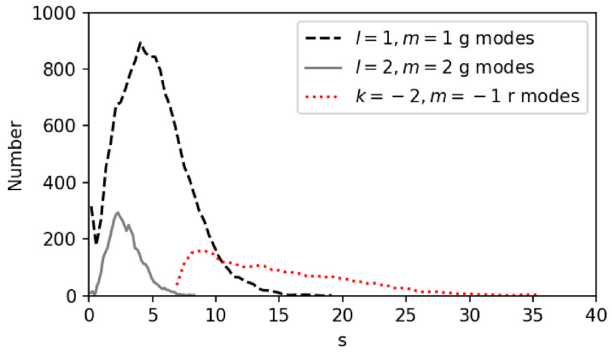

Figure 19. The spin parameter s distributions of $l = 1$, $m = 1$ g modes (black), $l = 2$, $m = 2$ g modes (grey), and $k = -2$, $m = -1$ r modes (red). Several extremely slowly rotating stars contribute the peak with s near 0 in $l = 1$, $m = 1$ g modes.

Bouabid et al. (2013) calculated the radial order span using the theory of mode stability and found the radial order span is typically 30. Our observed radial order span is longer than the theory, showing that improvement of the mode excitation and damping theory may be needed.

4.5 Distributions of spin parameters

Using equation (3), we calculate the spin parameters for $l = 1$, $m = 1$ g modes, $l = 2$, $m = 2$ g modes, and $k = -2$, $m = -1$ r modes. Fig. 19 displays their distributions. For $l = 1$, $m = 1$ g modes, the spin parameters show a rapid rise and a slow drop from 0 to 15. Most of the modes have s around 5. Several slow rotators have extremely low spin parameters, which form the peak close to zero. For $l = 2$, $m = 2$ g modes, the spin parameters are lower since the pulsation frequencies are longer than dipole g modes. Most of them are around 2.5. For r modes with $k = -2$, $m = -1$, they show different spin parameter distributions. The smallest spin parameter value is ∼6 and the highest is ∼35. They show a peak around 9. The r-mode spin parameters are typically larger than that of g modes and have different distributions, implying diverse pulsation properties for them.

5 ROTATION ON S–P DIAGRAM

5.1 Empirical method to calculate rotation rate

The fit of the TAR reveals the near-core rotation rate, asymptotic spacing, and the estimated radial orders of one pattern, given the quantum numbers k and m. This fitting procedure converges faster with a good initial estimate of $f_{\rm rot}$. Hence, we report an empirical method to estimate the near-core rotation rate based on the three observables: the mean period $\langle P \rangle$, the mean spacing $\langle \Delta P \rangle$, and the slope Σ. We use a simple formula to describe the relation between the near-core rotation rate and these three observables. The formula is designed as

$$f_{\rm rot} = \frac{A}{\langle P \rangle} + \frac{B}{\langle \Delta P \rangle} + C\,\Sigma + D, \quad (5)$$

where A, B, C, and D are the coefficients. We selected inversely proportional functions for $\langle P \rangle$ and $\langle \Delta P \rangle$ (both in unit of days) because they are inversely correlated with the rotation rate. For the slope Σ, the proportional relation is used since rapid rotation causes a steeper period-spacing pattern. On the left-hand side of

Table 2. The coefficients of equation (5) for $k = 0$, $m = 1$ g mode, $k = 0$, $m = 2$ g mode, and $k = -2$, $m = -1$ r mode. Note that $k = l - |m|$ for g modes. A, B, C, and D are the coefficients. $\delta f_{\rm rot}$ is the fitting accuracy in unit of d^{-1}.

(k, m)	A	B	C (d^{-1})	D (d^{-1})	$\delta f_{\rm rot}$ (d^{-1})
(0, 1)	0.4189	0.001603	− 11.75	− 0.3554	0.1
(0, 2)	0.3346	0.0003965	− 2.477	− 0.2462	0.07
(− 2, −1)	1.167	− 0.0002585	− 0.2360	0.1099	0.03

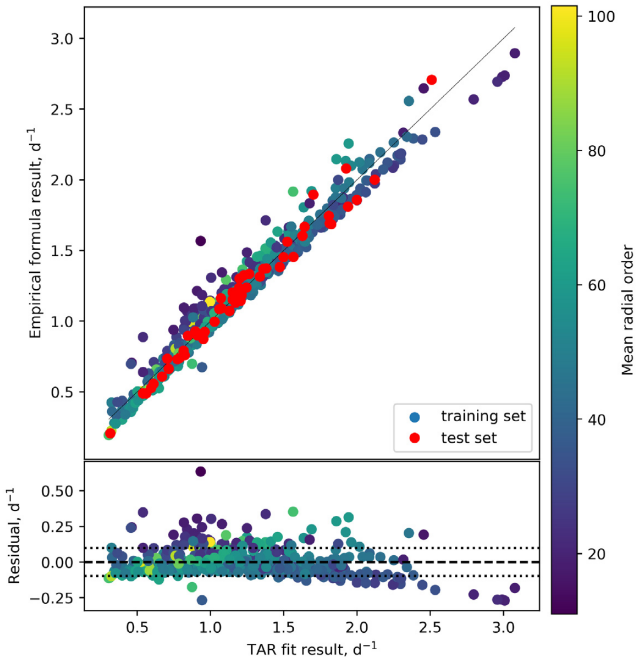

Figure 20. The near-core rotation rates calculated by equation (5) for $k = 0$, $m = 1$ g modes. Upper panel: the relation between the input and predicted near-core rotation rates. The red circles are the test set while the others are the training set. Lower panel: the fit residuals. The residuals have the standard deviation of $0.1\,\mathrm{d}^{-1}$, which is the accuracy of equation (5).

equation (5), the unit of $f_{\rm rot}$is d^{-1}. On the right-hand side, the coefficients A and B are dimensionless, the unit of coefficient C and D are d^{-1}. We applied equation (5) to $l = 1$, $m = 1$ g modes, $l = 2$, $m = 2$ g modes, and $k = -2$, $m = -1$ r modes, respectively. The slow rotators with $f_{\rm rot} < 0.4\,\mathrm{d}^{-1}$ were excluded, since the slope is affected by the glitches more than the rotational effect. The best-fitting coefficients are listed in Table 2.

Fig. 20 shows the fit result of $k = 0$, $m = 1$ g modes. The upper panel reveals the correlation of near-core rotation rates from the TAR fit and the empirical formula equation (5). We selected 90 per cent of the data points (coloured by their mean radial orders) as the training set to obtain the coefficients (listed in the first line of Table 2), and use the other 10 per cent (red circles) to test if the coefficients work well and to avoid overfitting. Both the training set and the test set show a positive correlation, which means that equation (5) with the parameters in Table 2 can estimate the near-core rotation rate. The lower panel shows the differences between the input and output rotation rates. The differences have a standard deviation of $0.1\,\mathrm{d}^{-1}$, which is the precision of equation (5) for $k = 0$, $m = 1$ g modes. We find that the mean radial orders show a gradient, in the sense that the points with small residuals have larger mean radial orders than those with large differences. Hence the scatter of equation (5) is partially caused by the mean radial order.

The second and third lines in Table 2 list the coefficients of equation (5) but for $k = 0$, $m = 2$ g modes and $k = -2$, $m = -1$ r modes. The precision of equation (5) for $k = 0$, $m = 2$ g modes is $0.07\,\mathrm{d}^{-1}$, which is similar to the $k = 0$, $m = 1$ g-mode residuals. However, The precision of $k = -2$, $m = -1$ r modes is $0.03\,\mathrm{d}^{-1}$, significantly smaller than those of g modes. The reason is that r modes are not affected by the range of radial orders as much as g modes.

Equation (5) with the coefficients in Table 2 gives the relation between the rotation rate and the three observables. They can be used as the estimate of the near-core rotation rate before running the TAR fit code. We also tried to search the formula for asymptotic spacing Π_0 and mean radial order as a function of $\langle P \rangle$, $\langle \Delta P \rangle$, and Σ, but there are no clear correlations.

5.2 Rotation on the S–P diagram

To plot the rotation rate on the S–P diagram, we used the TAR to simulate the period-spacing pattern and calculate the synthetic mean periods and slopes. We show our simulated curves in Fig. 21, whose parameters are listed in Table 3. For both g and r modes, the number of modes in each pattern was selected as 20 and the range of Π_0 is from 3600 to 5600 s with step of 200 s. For g modes, the rotation is between 0 and $4.0\,\mathrm{d}^{-1}$ with step of $0.1\,\mathrm{d}^{-1}$ to cover the observed range. Two regions of radial orders were used for g modes, centred at 20 ($10 < n < 30$) and 40 ($30 < n < 50$), as shown in blue and cyan lines in Fig. 21. For r modes, only radial orders around 20 ($10 < n < 30$) and $0.7\,\mathrm{d}^{-1} < f_{\rm rot} < 4.0\,\mathrm{d}^{-1}$ are displayed because these parameters regions can explain the r modes data well.

Fig. 21 shows the simulated results of the S–P diagram. We find that the simulated curves cover the data points well. For $l = 1$, $m = 1$ g modes, the data show two trends: one is the patterns with lower radial orders (the blue curves) which show shorter mean periods and the steeper relations between the slope and the period; another trend shows higher radial orders (cyan curves) whose mean periods are generally longer and the relation between the slope and the period is flatter. Two trends have an overlap over $P \sim 0.5$ d. For $l = 2$, $m = 2$ g modes, the trend between the slope and the mean period is not obvious due to the limited detection of quadrupole g modes. So only $10 < n < 30$ is used to cover $l = 2$, $m = 2$ g modes.

The S–P diagram is a map for the near-core rotation rate, as marked by the dashed lines and numbers in Fig. 21. The dashed lines connect the positions with same rotation rates, hence we can estimate the near-core rotation rate by placing the star on the S–P diagram. The rapidly rotating stars generally appear on the left in the S–P diagram, because of both the Coriolis force and the transformation between the corotating and inertial reference frame. The estimate of the near-core rotation rate is affected by the mode identification, the asymptotic spacing, and the radial orders. There is an overlapping area around $P \sim 0.5$ d. In this area, the pattern with higher radial order (cyan curves) shows a higher rotation rate ($\sim 1.6\,\mathrm{d}^{-1}$) while the pattern with low radial order (blue curves) has a slower rotation rate ($\sim 1\,\mathrm{d}^{-1}$). For r modes, the relation is clearer and the S–P map can give a better estimate for the near-core rotation rate. It also explains why the r-mode residuals in Table 2 are smaller than those for the g mode, since there is only one trend for r modes on the S–P diagram.

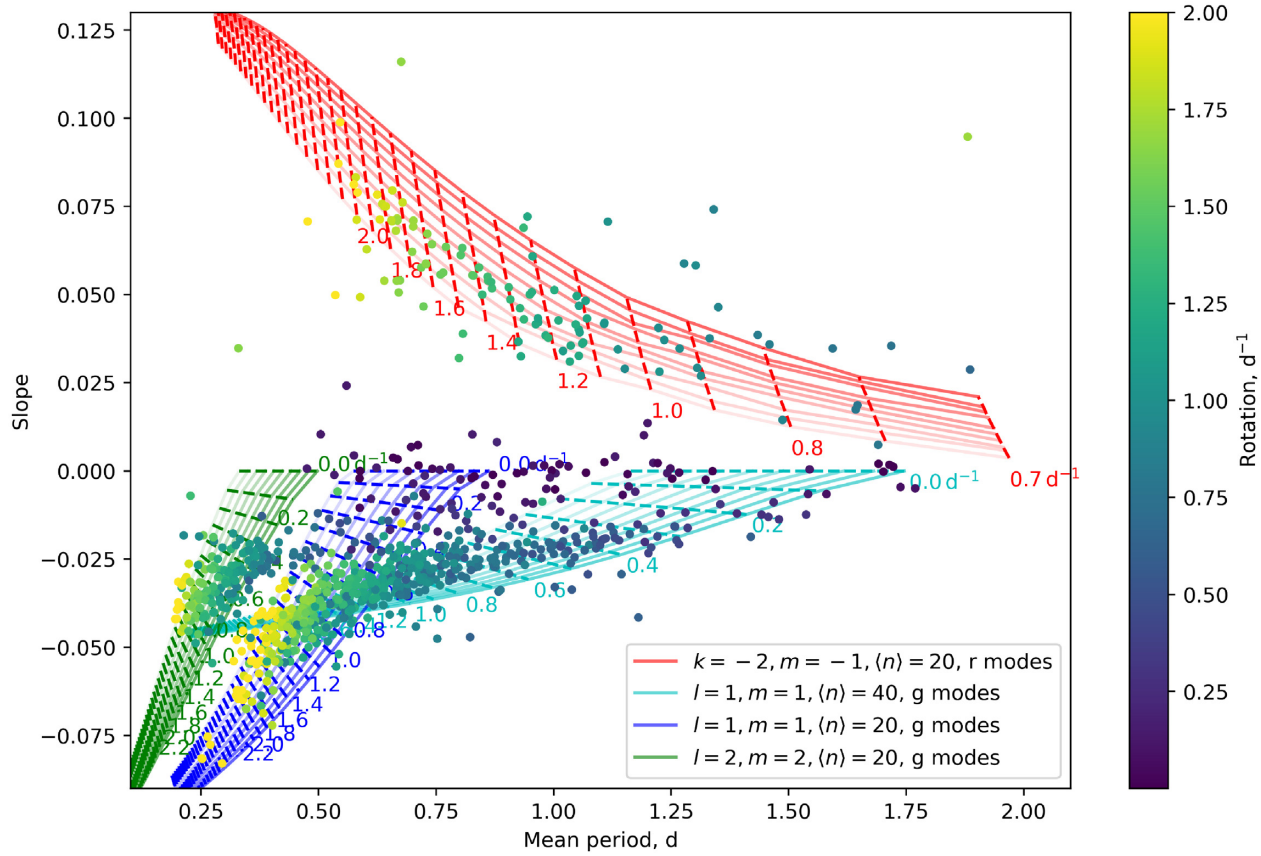

Figure 21. Theoretical S–P diagram. One solid line has the same quantum numbers, asymptotic spacing, and radial order centres with rotation increasing from right to left. The dashed lines connect the positions with same rotation rate. Different colours show the curves with different quantum numbers. The transparency stands for the asymptotic spacing Π_0. The lighter, the smaller the Π_0. The numbers show the rotation rates in d^{-1} of the nearest dashed lines. The parameters for those curves are listed in Table 3. The data points are coloured by their near-core rotation rates to make the comparison with the simulated rotation straightforward.

Table 3. The parameters of the simulated curvatures in Fig. 21. k and m are the quantum numbers of the modes. All the patterns have 20 modes with different radial order centres $\langle n \rangle$. Π_0 is the asymptotic spacing and $f_{\rm rot}$ is the near-core rotation rate.

Colour	(k, m)	$\langle n \rangle$	Π_0 (s) min, max, step	$f_{\rm rot}$ (d^{-1}) min, max, step
Blue	(0,1)	20	3600, 5600, 200	0.0, 4.0, 0.1
Cyan	(0,1)	40	3600, 5600, 200	0.0, 4.0, 0.1
Green	(0,2)	20	3600, 5600, 200	0.0, 4.0, 0.1
Red	(− 2, −1)	20	3600, 5600, 200	0.7, 4.0, 0.1

6 FAST ROTATORS WITH SPLITTINGS

Li et al. (2019a) reported 22 γ Dor stars in which rotational splittings were seen. The rotation rates of those stars are generally slow (with splitting smaller than 0.2 d^{-1}), hence their period-spacing patterns with different azimuthal orders m overlap each other. The traditional Échelle diagram was used to distinguish the patterns and the shift-copy method helped match the modes with equal radial order n (see details in Li et al. 2019a).

In this work, we found 11 stars whose splittings are much larger, whose mean splittings and slopes are listed in Table 4. Fig. 22 displays the splittings of KIC 7701947 as an example. The top panel shows the power spectrum, in which the red dots are the extracted frequencies and the open dots are the likely combination frequencies. We mark the $l = 1, m = 1$ g modes as the blue vertical lines and the $l = 1, m = 0$ g modes as the green vertical lines. The plus and circle symbols mark the locations of $m = 1$ and $m = 0$ modes, respectively. The horizontal dashed lines connect the modes with equal n. The bottom panel shows two period-spacing patterns, the left one (blue plus) is $l = 1$, $m = 1$ g modes and the right one (green circle) is $l = 1$, $m = 0$ g modes. The period-spacing patterns look similar to those in Fig. 1 but two features expose the difference:

Table 4. The slopes and splittings of 11 rapidly rotating stars. $\delta\nu$ are the mean splittings. $\Sigma_{l,m}$ are the slopes. The uncertainty on the last digit is given between brackets.

KIC	$\delta\nu$ (d^{-1})	$\Sigma_{l=1,m=1}$	$\Sigma_{l=1,m=0}$
3348714	0.38(2)	− 0.0352(2)	− 0.0154(4)
4285040	0.46(2)	− 0.014(4)	− 0.0163(3)
4846809	0.65(1)	− 0.036(6)	− 0.0087(7)
4952246	0.316(9)	− 0.005(5)	− 0.011(1)
5476473	1.00(2)	− 0.055(5)	− 0.0148(8)
7701947	0.32(1)	− 0.0281(1)	− 0.0165(5)
7778114	0.50(2)	− 0.0355(5)	− 0.0202(2)
8523871	0.32(5)	− 0.075(5)	− 0.067(7)
9595743	0.42(1)	− 0.044(4)	− 0.027(7)
12102187	0.291(6)	− 0.017(7)	− 0.019(9)
12401800	0.43(1)	− 0.0308(8)	− 0.021(1)

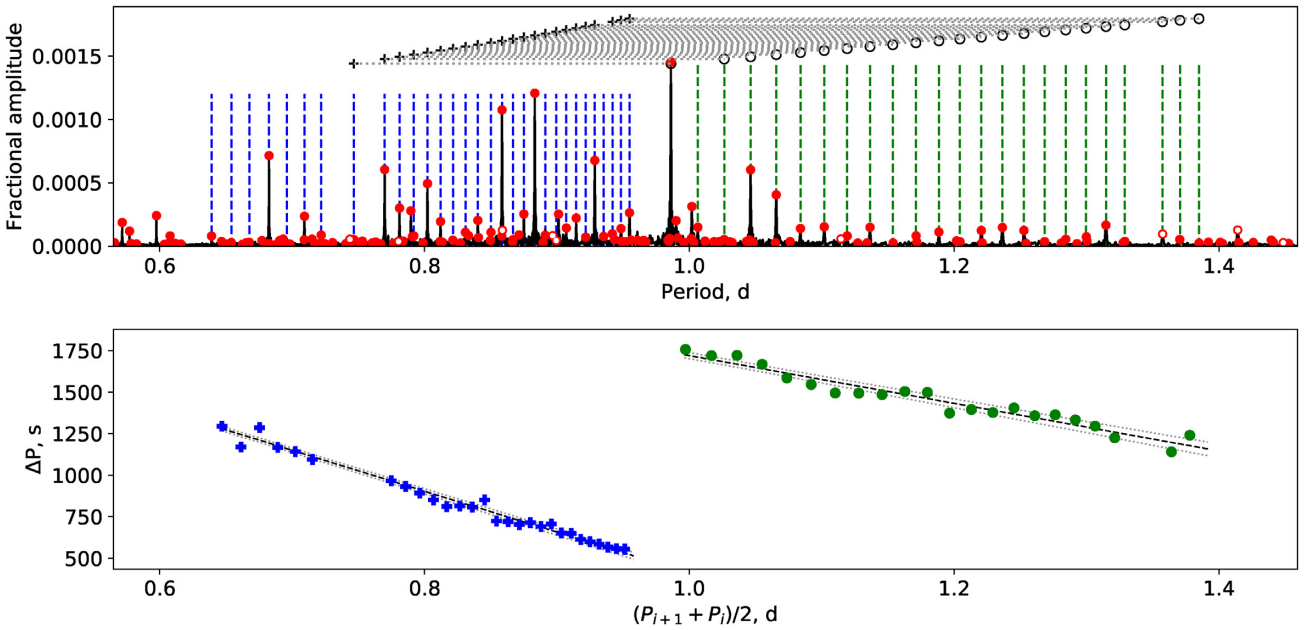

Figure 22. The amplitude spectrum and period-spacing patterns of KIC 7701947. Top panel: the amplitude spectrum as a function of period. The red dots are the extracted frequencies and the open dots show the likely combination frequencies. The vertical dashed lines show the linear fit by equation (1). Two period-spacing patterns are seen. The left one denoted by the blue dashed lines is the $l = 1$, $m = 1$ g modes. The right one (green vertical lines) is the $l = 1$, $m = 0$ g modes. Above the spectrum ' + ' is the $m = 1$ modes and 'O' is the $m = 0$ modes. The horizontal dotted lines connect the modes with same radial order n. Bottom: the period-spacing patterns. The left one is the $l = 1$, $m = 1$ g modes while the right one is $l = 1$, $m = 0$ g modes. The linear fits and uncertainties are shown by the black and grey dashed lines, with dips removed.

(i) the ratio of pulsation periods between $m = 1$ and $m = 0$ modes does not have a factor of two.

(ii) Slopes of $m = 1$ and $m = 0$ modes are different so the patterns are not parallel.

We also state that these splitting stars are not binaries, since we can use the same parameters ($\Pi_0, f_{\rm rot}$) to fit both the patterns ($m = 1$ or $m = 0$) in each star.

Under the condition of slow rotation, the dipole ($l = 1$) g-mode splitting is calculated based on the first-order perturbation

$$\delta f = f_{n,l=1,\ m=1} - f_{n,l=1,\ m=0} = m\left(1 - C_{n,l}\right) f_{\rm rot}, \tag{6}$$

where f is the pulsation frequency, $C_{n,\,l} \simeq 1/[l(l+1)] = 0.5$ is the Ledoux constant, $f_{\rm rot}$ is the near-core rotation rate (Ledoux 1951), the term m is one since we consider dipole g modes. We only consider the splitting between $m = 1$ and $m = 0$ modes since $m = -1$ retrograde modes are absent in the fast rotating stars (see theory in e.g. Saio et al. 2018b). However, the perturbation is broken with increasing rotation rate. For the newly discovered splitting stars with much faster rotation rates, the splittings vary between different overtones significantly and it is hard to match the modes with the same n.

For the fast rotators, the TAR in equation (2) is a good approximation. The frequency in the corotating frame is

$$f_{nlm,\rm co} = \frac{\sqrt{\lambda_{l,m,s}}}{\Pi_0\left(n + \varepsilon_g\right)}, \tag{7}$$

whose variables are same as equation (2). The frequency in the inertial frame is

$$f_{nlm,\rm in} = f_{nlm,\rm co} + m f_{\rm rot}, \tag{8}$$

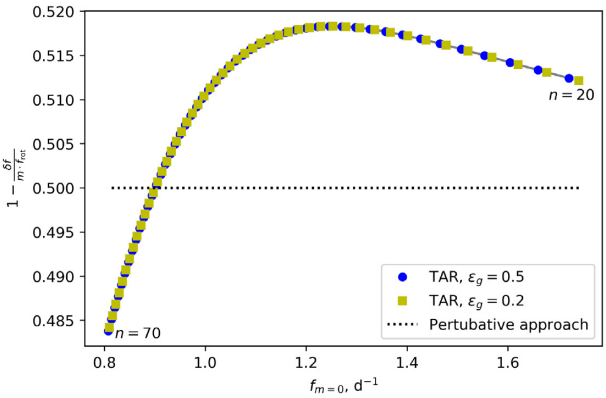

Figure 23. The theoretical Ledoux 'constant' as a function of frequency from the TAR, with $\Pi_0 = 4000$ s and $f_{\rm rot} = 1\,{\rm d}^{-1}$. The considered radial orders have values between 20 and 70. The blue circles and yellow squares show the 'constant' with different ε_g. The horizontal dotted line denotes the position with $C_{n,\,l} = 0.5$.

where $f_{\rm rot}$ is the near-core rotation rate. Therefore the splittings is calculated by

$$\delta f = m f_{\rm rot} + \frac{1}{\Pi_0\left(n + \varepsilon_g\right)}\left(\sqrt{\lambda_{l,m=1,s}} - \sqrt{\lambda_{l,m=0,s'}}\right). \tag{9}$$

Hence the Ledoux 'constant' $C = 1 - \delta f/(m f_{\rm rot})$ is no longer a 'constant' (see also Keen et al. 2015; Murphy et al. 2016). Fig. 23 shows the theoretical result of the varying Ledoux 'constant'. The parameters are $\Pi_0 = 4000$ s and $f_{\rm rot} = 1\,{\rm d}^{-1}$, which are chosen from the distributions shown in Figs 9 and 13. We find that with increasing pulsation frequency, the Ledoux 'constant' increases from ~0.485, reaches the highest value around 0.52, and drops

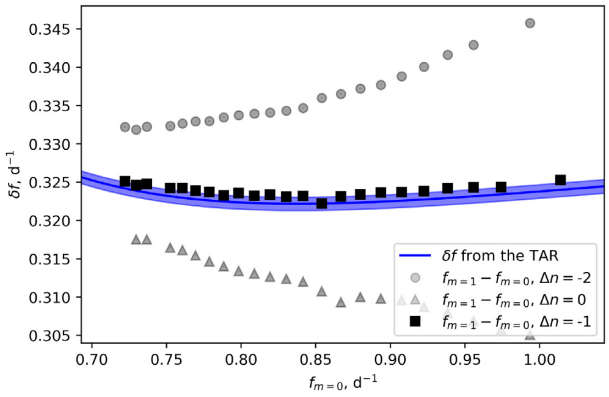

Figure 24. The splitting variation as a function of frequency of KIC 7701947. The blue line and shaded area are the predicted curve and uncertainty from the TAR fitting result. The black squares are the splittings which follow the theory best, whose radial orders are subtracted by 1 artificially for the best-fitting result. The grey circles and triangles are the splittings whose radial orders are mismatched by a factor of ±1 around −1.

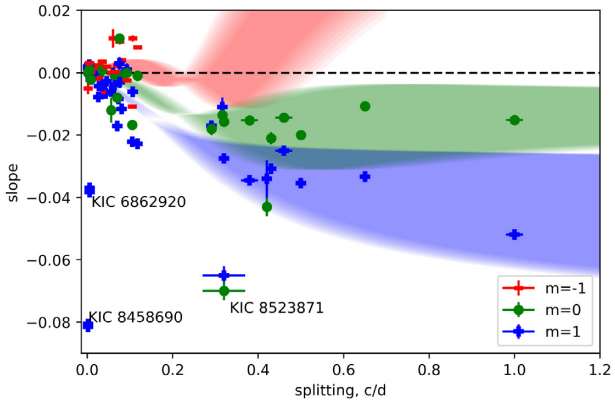

Figure 25. Observed relation between slope and splitting from 34 stars. The shaded areas are theoretical curves. We consider the radial orders from 20 to 70 to make the theoretical areas. KIC 6862920 and KIC 8458690 are binaries, KIC 8523871 shows a much larger asymptotic spacing, hence they become outliers.

slowly. The deviation from the first-order perturbation is ∼±0.02. We also evaluated different values for ε_g and find that it does not change the curve, but only shifts the frequencies of zonal modes, as shown by the blue circles and yellow squares in Fig. 23.

Fig. 24 shows the comparison between the observed splittings and the theoretical predictions of KIC 7701947. The blue curve and shaded area show the theoretical splittings and uncertainties, whose parameters are from the best-fitting TAR result. We tried to introduce an artificial shift on the radial order of the $l = 1, m = 0$ g modes and plot the results as grey circles and triangles in Fig. 24. The black squares are the matching that follows the theory best. We find that changing the mode matching by $\Delta n = \pm 1$ indeed changes the shape of splitting. The splittings with correct matching generally follow the theoretical prediction. However, the observed splittings are higher than the theoretical one, showing a discrepancy with the theory. It means the best model which fits the period-spacing patterns can only partly explain the splittings. This reflects the limit of the asymptotic formula of the TAR in equation (2), which can be improved by performing a full seismic calculation.

Ouazzani et al. (2017) showed that the near-core rotation can be deduced roughly by the slope. To make an observed relation between rotation and slope, we combined the 11 rapidly rotating stars with splittings and 22 slow rotating stars from Li et al. (2019a) to extend the observed slope–splitting diagram to a larger splitting area. Fig. 25 shows the slope–splitting relation with both the observations and theoretical curves. The observed points cluster into two groups: the left one is composed of the slow rotators with splitting smaller than 0.2 d^{-1} and slope close to 0, while the points with splitting larger than 0.2 d^{-1} are the fast rotators. There is a gap over 0.2 d^{-1}, which corresponds to the boundary between the slow and fast rotators in Section 4.2. Due to the effect of rotation, the slopes of the fast rotators deviate from zero and become lower than the slow rotators. The slopes of zonal modes (green) are generally flatter than the slopes of dipole sectoral modes (blue), consistent with the theoretical curves by Ouazzani et al. (2017) and us. The retrograde modes (red) are only seen in the slow rotators. The reasons of the absence of retrograde modes in fast rotators are: (1) the period spacings are around 10^4 s, hence they are hard to detect; (2) the amplitudes of retrograde modes are concentrated to the equator; (3) an additional latitudinal nodal lines appear when $s > 1$, hence retrograde modes become tesseral modes. Therefore, no retrograde modes are expected in fast rotators (Saio et al. 2018b).

The shaded areas are the theoretical regions of slopes as a function of splittings with different modes. We calculated the simulated period-spacing patterns by the TAR, and measured the slopes of them. The asymptotic spacing Π_0 is from 3500 to 4500 s with step of 100 s. The radial order is from 20 to 70. Since the period spacing changes quasi-linearly with period, the slope changes as a function of radial order. We measured the slope at the beginning and at the end of each simulated period-spacing pattern. We found that the slope variation at different radial orders is significant, hence the slope–splitting curves in our work show a much larger dispersion than Ouazzani et al. (2017), who neglected this effect. Our simulated curves in Fig. 25 cover the data points in the fast rotation area, but have difficulty in the slow rotation area. The slopes of slowly rotating stars spread much wider than the shaded area, implying that dips dominate the measurement of slopes in slowly rotating stars.

We only see 11 rapidly rotating stars with splittings among 611 γ Dor stars in our sample. The lack may reflect the surface amplitude distribution of tesseral modes. With increasing rotation, the mode geometry are concentrated towards the equator, hence the brightness change by pulsations is cancelled out unless the line of sight is almost aligned with the rotation axis of the star (Townsend 2003b). Apart from these 11 splitting stars, we also find two stars, KIC 5092684 and KIC 5544996, which show $l = 2, m = 1$ modes. Precise observations of their projected equatorial velocities $v \sin i$ will reveal their inclinations and allow us to evaluate the theoretical expectations for the amplitude distributions of the pulsation modes.

7 SURFACE MODULATIONS

The g and r modes allow us to measure the rotation rate of the near-core region. To see how the rotation rate changes radially, which is crucial to understand the angular momentum transfer, we looked for the surface modulation signals. The surface modulation might be caused by spots (e.g. McQuillan, Mazeh & Aigrain 2014), or stellar activities, which is straightforward to detect since the signal is located within the typical g-mode period region. Although we

excluded the eclipsing binaries (EB) when selecting the stars, there are still several stars which were classified as EB by Kirk et al. (2016), since their eclipses are too shallow to be seen in the time domain. The orbital periods are equal to the surface rotation periods for short-period EBs, considering the components are tidally locked. Hence we can use the orbital period as the surface rotation period. We follow the criteria used by Van Reeth et al. (2018) and Li et al. (2019b) to select the rotational modulation signal. The criteria are:

(i) the surface modulation is a closely spaced group of peaks in the amplitude spectrum, assuming the lifetime of spot is shorter than the 4-yr observation.
(ii) the S/N is larger than 4.
(iii) the harmonic of the highest peak is seen.
(iv) the signal is located between g and r modes. For those without r modes, we search the signal between one and two times the g-mode mean period, because the mean period of r modes is approximately twice the mean period of g modes.
(v) Both the rotational modulation signal at the rotation frequency and its harmonic have to be well separated from the period-spacing patterns, to avoid mistaking pulsation modes for rotational modulation.

We find 58 stars which show surface modulations, representing about 9.5 per cent of the 611 stars. The fraction is consistent with spectroscopic observations of Zeeman splitting (Donati & Landstreet 2009; Wade et al. 2016) and previous photometric observations of smaller samples (Van Reeth et al. 2018; Li et al. 2019b). Table 5 lists the KIC numbers of these stars, the near-core ($f_{\rm core}$), and surface ($f_{\rm surf}$) rotation rates, and their ratios. Fig. 26 gives the amplitude spectrum of KIC 5608334 which shows a surface rotation signal. We find a peak group at ∼0.44 d (red dashed line), which is consistent with the near-core rotation rate derived by the g-mode period-spacing pattern. A hump in Fig. 26 appears around 0.5 d, which we identify as unresolved r modes (e.g. Saio et al. 2018a).

However, not all such humps are r modes. Fig. 27 displays the surface modulation of KIC 5608334, in which the hump at ∼0.52 d lies over the near-core rotation period. This hump is not unresolved r modes since the latter have periods longer than the rotation period. We conclude that this hump is caused by the spots on the surface, as pointed out by e.g. Balona (2013).

We calculate the ratio between the near-core and surface rotation and show them in Fig. 28. We find that almost all the stars rotate nearly rigidly since the ratio is between 0.95 and 1.08. The distribution shows a sharp drop at ∼0.99, implying that the near-core region rotates slightly faster than the surface, which is consistent with the theoretical rotation profile reported by Rieutord (2006). A possible selection bias needs to be mentioned. A surface rotation period longer than the near-core rotation period might not be detected since this signal may be identified as a peak group of unresolved r modes.

Table 5. The near-core and surface rotation rates, and their ratios of 58 stars which show surface modulation signals. 'EB' means the star is an eclipsing binary and 'SURF' means the signal is caused by surface modulations. $f_{\rm core}$ is the near-core rotation rate and $f_{\rm surf}$ is the surface rotation rate.

KIC	Type	$f_{\rm core}$ (d^{-1})	$f_{\rm surf}$ (d^{-1})	$f_{\rm core}/f_{\rm surf}$
KIC 2846358	SURF	0.755(4)	0.754(8)	1.00(1)
KIC 3341457	EB	1.859(1)	1.893(7)	0.982(4)
KIC 3440840	SURF	0.93(6)	0.938(7)	0.99(6)
KIC 3967085	SURF	0.76(2)	0.77(1)	1.00(3)
KIC 4171102	SURF	0.7579(6)	0.76(2)	1.00(2)
KIC 4567531	SURF	1.018(5)	0.94(2)	1.08(2)
KIC 4932417	SURF	1.285(8)	1.23(2)	1.05(2)
KIC 4951030	SURF	2.53(3)	2.49(4)	1.02(2)
KIC 5021329	SURF	2.02(2)	1.98(4)	1.02(2)
KIC 5025464	SURF	1.57(3)	1.561(3)	1.00(2)
KIC 5115637	SURF	0.714(6)	0.72(2)	0.99(2)
KIC 5210153	SURF	1.051(4)	1.040(5)	1.011(6)
KIC 5370431	SURF	0.618(5)	0.6122(6)	1.009(8)
KIC 5374279	SURF	1.00(2)	0.873(4)	1.14(3)
KIC 5608334	SURF	2.25(1)	2.241(3)	1.005(6)
KIC 5652678	SURF	1.140(5)	1.163(6)	0.980(6)
KIC 5876187	SURF	0.596(5)	0.584(4)	1.02(1)
KIC 5954264	SURF	1.330(9)	1.329(6)	1.001(8)
KIC 5978913	SURF	0.955(5)	0.950(6)	1.006(8)
KIC 6041803	EB	1.53(2)	1.524(7)	1.00(1)
KIC 6284209	SURF	1.48(2)	1.42(4)	1.04(3)
KIC 6366512	SURF	1.17(1)	1.18(1)	0.99(1)
KIC 6445969	SURF	1.263(7)	1.244(5)	1.015(7)
KIC 6469690	SURF	0.566(5)	0.554(6)	1.02(1)
KIC 6935014	SURF	0.789(3)	0.788(7)	1.00(1)
KIC 7059699	SURF	2.30(2)	2.27(2)	1.01(1)
KIC 7287165	SURF	0.95(1)	0.986(2)	0.96(1)
KIC 7344999	SURF	1.40(1)	1.40(3)	1.00(2)
KIC 7434470	EB	1.77(1)	1.698(1)	1.044(6)
KIC 7596250	EB	1.1876(7)	1.185(4)	1.003(4)
KIC 7620654	SURF	1.88(2)	1.83(4)	1.03(2)
KIC 7621649	SURF	0.7745(4)	0.7802(6)	0.9928(9)
KIC 7840642	SURF	1.158(6)	1.158(6)	1.000(8)
KIC 7968803	SURF	1.94(1)	1.949(7)	0.997(8)
KIC 8180062	SURF	0.907(5)	0.904(9)	1.00(1)
KIC 8197019	SURF	1.89(5)	1.86(4)	1.01(3)
KIC 8264667	SURF	0.684(5)	0.682(2)	1.002(8)
KIC 8264708	SURF	1.636(1)	1.636(1)	1.000(1)
KIC 8293692	SURF	1.00(2)	1.044(9)	0.95(2)
KIC 9573582	SURF	0.9495(5)	0.946(5)	1.004(6)
KIC 9652302	SURF	0.9147(6)	0.910(2)	1.005(3)
KIC 9716350	SURF	0.863(3)	0.864(1)	0.999(3)
KIC 9716563	SURF	0.9081(9)	0.90(2)	1.01(2)
KIC 9847243	SURF	0.933(5)	0.913(9)	1.02(1)
KIC 10347481	SURF	1.303(5)	1.27(2)	1.03(2)
KIC 10423501	SURF	0.8420(6)	0.841(4)	1.001(4)
KIC 10470294	SURF	2.00(2)	1.96(4)	1.02(2)
KIC 10483230	SURF	0.9126(4)	0.918(2)	0.995(2)
KIC 10669515	SURF	1.596(7)	1.567(4)	1.019(5)
KIC 10803371	EB	0.98(2)	1.011(3)	0.97(2)
KIC 11183399	SURF	1.89(2)	1.868(3)	1.01(1)
KIC 11201483	SURF	2.28(2)	2.23(3)	1.02(2)
KIC 11294808	SURF	0.802(5)	0.7887(7)	1.016(7)
KIC 11395936	EB	0.944(7)	0.953(6)	0.99(1)
KIC 11462151	SURF	2.00(2)	1.93(4)	1.03(2)
KIC 11520274	SURF	1.03(2)	1.025(3)	1.00(2)
KIC 11922283	SURF	1.088(8)	1.07(1)	1.02(1)
KIC 12202137	SURF	1.96(1)	1.96(1)	0.998(8)

8 CONCLUSIONS

We report 960 period-spacing patterns detected from 611 γ Dor stars, including 22 slow rotators with rotational splittings, 11 rapid rotators with rotational splittings, 110 stars with r modes, and 58 stars that present surface modulation signals. The majority (62.0 per cent) of the detected modes are $l = 1$, $m = 1$ g modes. We also see many $l = 2$, $m = 2$ g modes and $k = -2$, $m = -1$ Rossby modes, which comprise 18.9 per cent and 11.5 per cent of the sample, respectively. Among the 611 γ Dor stars, there are 339 stars which only show dipole g modes, 145 stars showing both dipole and quadrupole g modes, 83 stars showing dipole g modes and $k = -2$, $m = -1$ r modes, 27 stars showing dipole, quadrupole g modes, and r modes. We also find 16 stars whose dipole g modes cannot be resolved, and one star which does not show any dipole g-mode power.

For each pattern, a series of pulsation periods were identified. The mean periods, the mean period spacings, and the slope were

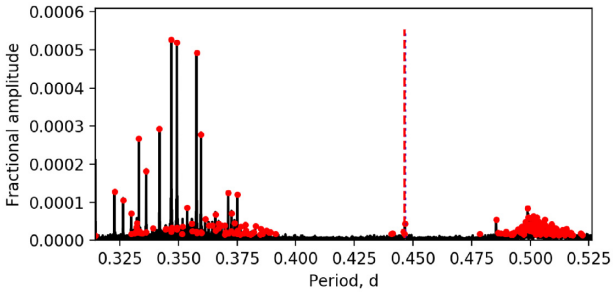

Figure 26. The near-core and surface rotations of KIC 5608334. The red dots show the frequencies. The red dashed line shows the surface rotation period, which is consistent with the near-core rotation rate derived by the g-mode pattern. The hump at 0.5 d is the unsolved r modes.

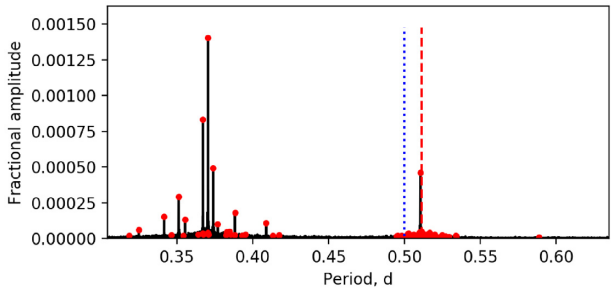

Figure 27. Same as Fig. 26 but for KIC 10470294. The red vertical dashed line shows the surface rotation period while the blue dotted line gives the near-core rotation rate. We identify that in this star the hump at 0.52 d is the surface rotation signal, not r modes.

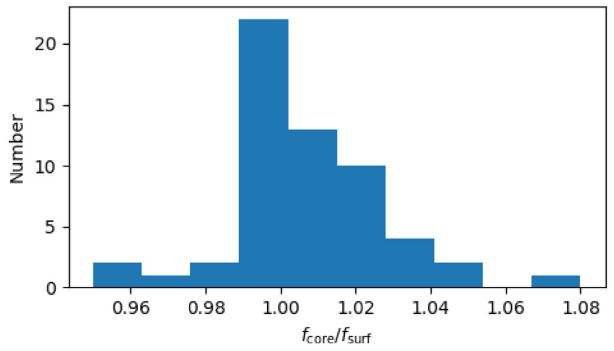

Figure 28. The distributions of the core-to-surface rotation ratio.

calculated for each pattern. We find γ Dor stars have a relation on the slope–mean period diagram (S–P diagram, Fig. 8), where the data points cluster into different areas based on their quantum numbers. The S–P diagram gives the typical pulsation period and slopes of γ Dor stars. For $l = 1$, $m = 1$ g modes, the periods are between 0.3 and 1.2 d with a slope around -0.03, while for $l = 2$, $m = 2$ g modes, the period is half that of the $l = 1$, $m = 1$ g modes but the slope is similar. Both $l = 2$, $m = 2$ and $l = 1$, $m = 1$ g modes show a positive correlation between the slope and the mean period, which is an effect of rotation confirmed by the TAR simulations.

We obtain the near-core rotation rates, the asymptotic spacings, and the radial orders using the TAR. We find that the distribution of the near-core rotation rate shows a slow-rotator excess, similar to the previous observations of the projected velocity $v \sin i$. There are more slow rotators than the angular momentum transfer models by Ouazzani et al. (2018) predicted, implying some additional mechanisms of angular momentum transfer are present inside these stars, or the effect of overshooting is significant. We obtained 11 fast rotators that show splittings, whose modes are $l = 1$, $m = 1$ and $l = 1$, $m = 0$ g modes. Due to the rapid rotation, the splitting varies as a function of radial order. We find that the best-fitting TAR result can explain the period-spacing patterns but it can only partly explain the splittings. Surface modulations are found in 58 stars, with rotation rates close to the near-core rotation rates. Most γ Dor stars rotate rigidly, with the near-core region rotating slightly faster, but not by more than 5 per cent.

Our observational sample is large enough to identify some outstanding problems in theoretical models of γ Dor stars:

(i) Most stars in the γ Dor instability strip do not show period-spacing patterns, or their patterns are incomplete. Mode selection mechanisms for γ Dor pulsations are needed.

(ii) Concerning γ Dor pulsation excitation, we confirm that a number of γ Dor stars have hotter temperatures and also excite more radial orders than theoretically predicted.

(iii) We observe that the near-core regions of γ Dor stars rotate more slowly than expected, in disagreement with the theory. Two directions might be considered: fast rotation hinders g-mode pulsations, or our model for angular momentum transport is missing some key mechanisms.

ACKNOWLEDGEMENTS

The research was supported by an Australian Research Council DP grant DP150104667. Funding for the Stellar Astrophysics Centre is provided by the Danish National Research Foundation (Grant agreement no.: DNRF106). TVR has received funding from the European Research Council (ERC) under the European Union's Horizon 2020 research and innovation programme (grant agreement N°670519: MAMSIE) and from the KU Leuven Research Council (grant C16/18/005: PARADISE). This work has made use of data from the European Space Agency (ESA) mission *Gaia* (https://www.cosmos.esa.int/gaia), processed by the *Gaia* Data Processing and Analysis Consortium (DPAC, https://www.cosmos.esa.int/web/gaia/dpac/consortium). Funding for the DPAC has been provided by national institutions, in particular the institutions participating in the *Gaia* Multilateral Agreement.

REFERENCES

Abt H. A., Morrell N. I., 1995, ApJS, 99, 135
Asplund M., Grevesse N., Sauval A. J., Scott P., 2009, ARA&A, 47, 481
Balona L. A., 2013, MNRAS, 431, 2240
Balona L. A., Krisciunas K., Cousins A. W. J., 1994, MNRAS, 270, 905
Borucki W. J. et al., 2010, Science, 327, 977
Bouabid M.-P., Montalbán J., Miglio A., Dupret M.-A., Grigahcène A., Noels A., 2009, in Guzik J. A., Bradley P. A., eds, AIP Conf. Proc. Vol. 1170, Stellar Pulsation: Challenges For Theory and Observation. Am. Inst. Phys., New York, p. 477
Bouabid M.-P., Dupret M.-A., Salmon S., Montalbán J., Miglio A., Noels A., 2013, MNRAS, 429, 2500
Ceillier T., Eggenberger P., García R. A., Mathis S., 2013, A&A, 555, A54
Chowdhury S., Joshi S., Engelbrecht C. A., De Cat P., Joshi Y. C., Paul K. T., 2018, Ap&SS, 363, 260
Christophe S., Ballot J., Ouazzani R.-M., Antoci V., Salmon S. J. A. J., 2018, A&A, 618, A47
Donati J.-F., Landstreet J. D., 2009, ARA&A, 47, 333
Dupret M.-A., Grigahcène A., Garrido R., Gabriel M., Scuflaire R., 2005, A&A, 435, 927

Eckart C., 1960, Hydrodynamics of Oceans and Atmospheres. Pergamon Press, Oxford
Eggenberger P., Montalbán J., Miglio A., 2012, A&A, 544, L4
Fukuda I., 1982, PASP, 94, 271
Fulcher B. D., Jones N. S., 2017, Cell Syst., 5, 527
Fulcher B. D., Little M. A., Jones N. S., 2013, J. R. Soc. Interface, 10, 20130048
Fuller J., Piro A. L., Jermyn A. S., 2019, MNRAS, 485, 3661
Gaia Collaboration, 2016, A&A, 595, A1
Grassitelli L., Fossati L., Langer N., Miglio A., Istrate A. G., Sanyal D., 2015, A&A, 584, L2
Groot P. J., Piters A. J. M., van Paradijs J., 1996, A&AS, 118, 545
Guo Z., Gies D. R., Matson R. A., 2017, ApJ, 851, 39
Guzik J. A., Kaye A. B., Bradley P. A., Cox A. N., Neuforge C., 2000, ApJ, 542, L57
Hut P., 1981, A&A, 99, 126
Kallinger T. et al., 2017, A&A, 603, A13
Kaye A. B., Handler G., Krisciunas K., Poretti E., Zerbi F. M., 1999, PASP, 111, 840
Keen M. A., Bedding T. R., Murphy S. J., Schmid V. S., Aerts C., Tkachenko A., Ouazzani R.-M., Kurtz D. W., 2015, MNRAS, 454, 1792
Kirk B. et al., 2016, AJ, 151, 68
Koch D. G. et al., 2010, ApJ, 713, L79
Kurtz D. W., Saio H., Takata M., Shibahashi H., Murphy S. J., Sekii T., 2014, MNRAS, 444, 102
Ledoux P., 1951, ApJ, 114, 373
Lee U., Saio H., 1987, MNRAS, 224, 513
Lee U., Saio H., 1997, ApJ, 491, 839
Li G., Bedding T. R., Murphy S. J., Van Reeth T., Antoci V., Ouazzani R.-M., 2019a, MNRAS, 482, 1757
Li G., Van Reeth T., Bedding T. R., Murphy S. J., Antoci V., 2019b, MNRAS, 487, 782
Maeder A., 2009, Physics, Formation and Evolution of Rotating Stars, Springer, Berlin, Heidelberg
Mathis S., Decressin T., Eggenberger P., Charbonnel C., 2013, A&A, 558, A11
Mathur S. et al., 2017, ApJS, 229, 30
Mazumdar A. et al., 2014, ApJ, 782, 18
McQuillan A., Mazeh T., Aigrain S., 2014, ApJS, 211, 24
Mestel L., 1968, MNRAS, 138, 359
Mombarg J. S. G., , Van Reeth T., Pedersen M. G., Molenberghs G., Bowman D. M., Johnston C., Tkachenko A., Aerts C., 2019, MNRAS, 485, 3248
Mosser B. et al., 2012, A&A, 548, A10
Murphy S. J., Shibahashi H., Kurtz D. W., 2013, MNRAS, 430, 2986
Murphy S. J., Fossati L., Bedding T. R., Saio H., Kurtz D. W., Grassitelli L., Wang E. S., 2016, MNRAS, 459, 1201
Murphy S. J., Moe M., Kurtz D. W., Bedding T. R., Shibahashi H., Boffin H. M. J., 2018, MNRAS, 474, 4322
Murphy S. J., Hey D., Van Reeth T., Bedding T. R., 2019, MNRAS, 485, 2380
Ouazzani R.-M., Salmon S. J. A. J., Antoci V., Bedding T. R., Murphy S. J., Roxburgh I. W., 2017, MNRAS, 465, 2294
Ouazzani R.-M., Marques J. P., Goupil M., Christophe S., Antoci V., Salmon S. J. A. J., 2019, A&A, 626, A121
Papaloizou J., Pringle J. E., 1978, MNRAS, 182, 423
Pápics P. I., Tkachenko A., Aerts C., Van Reeth T., De Smedt K., Hillen M., Østensen R., Moravveji E., 2015, ApJ, 803, L25
Pápics P. I. et al., 2017, A&A, 598, A74
Paxton B., Bildsten L., Dotter A., Herwig F., Lesaffre P., Timmes F., 2011, ApJS, 192, 3
Paxton B. et al., 2013, ApJS, 208, 4
Paxton B. et al., 2015, ApJS, 220, 15
Paxton B. et al., 2018, ApJS, 234, 34
Provost J., Berthomieu G., Rocca A., 1981, A&A, 94, 126
Ramella M., Boehm C., Gerbaldi M., Faraggiana R., 1989, A&A, 209, 233
Rieutord M., 2006, A&A, 451, 1025
Royer F., Zorec J., Gómez A. E., 2007, A&A, 463, 671
Saio H., 1982, ApJ, 256, 717
Saio H., Kurtz D. W., Takata M., Shibahashi H., Murphy S. J., Sekii T., Bedding T. R., 2015, MNRAS, 447, 3264
Saio H., Kurtz D. W., Murphy S. J., Antoci V. L., Lee U., 2018a, MNRAS, 474, 2774
Saio H., Bedding T. R., Kurtz D. W., Murphy S. J., Antoci V., Shibahashi H., Li G., Takata M., 2018b, MNRAS, 477, 2183
Shibahashi H., 1979, PASJ, 31, 87
Stumpe M. C., Smith J. C., Catanzarite J. H., Van Cleve J. E., Jenkins J. M., Twicken J. D., Girouard F. R., 2014, PASP, 126, 100
Takada-Hidai M., Kurtz D. W., Shibahashi H., Murphy S. J., Takata M., Saio H., Sekii T., 2017, MNRAS, 470, 4908
Townsend R. H. D., 2003a, MNRAS, 340, 1020
Townsend R. H. D., 2003b, MNRAS, 343, 125
Townsend R. H. D., 2005, MNRAS, 360, 465
Triana S. A., Moravveji E., Pápics P. I., Aerts C., Kawaler S. D., Christensen-Dalsgaard J., 2015, ApJ, 810, 16
Van Reeth T. et al., 2015, ApJS, 218, 27
Van Reeth T., Tkachenko A., Aerts C., 2016, A&A, 593, A120
Van Reeth T. et al., 2018, A&A, 618, A24
Wade G. A., Petit V., Grunhut J. H., Neiner C., MiMeS Collaboration, 2016, in Sigut T. A. A., Jones C. E., eds, ASP Conf. Ser. Vol. 506, Bright Emissaries: Be Stars as Messengers of Star-Disk Physics. Astron. Soc. Pac., San Francisco, p. 207
Xiong D. R., Deng L., Zhang C., Wang K., 2016, MNRAS, 457, 3163
Zahn J.-P., 1992, A&A, 265, 115
Zhang X. B., Fu J. N., Luo C. Q., Ren A. B., Yan Z. Z., 2018, ApJ, 865, 115

SUPPORTING INFORMATION

Supplementary data are available at *MNRAS* online.

We present four appendices: period-spacing patterns and TAR fittings, parameters of the γ Dor stars, 11 rapidly rotating stars with rotational splittings, and 58 stars with surface rotation signals. The appendices are online only, here we only give the descriptions.

Appendix A. Period-Spacing Patterns And Tar Fits.
Appendix B. Parameters Of The γ Dor Stars.
Appendix C. Rapidly Rotating Stars With Rotational Splittings.
Appendix D. Surface Modulations Of 58 Stars.

Please note: Oxford University Press is not responsible for the content or functionality of any supporting materials supplied by the authors. Any queries (other than missing material) should be directed to the corresponding author for the article.

APPENDIX A: PERIOD-SPACING PATTERNS AND TAR FITS

We present the periodograms and period-spacing patterns of 611 γ Dor stars. For each star, we show the periodogram with identified modes, the period-spacing pattern(s) and the linear fitting(s), and sideways Échelle diagram(s). We also show the TAR fitting and the posterior distributions of the near-core rotation rate and the asymptotic spacing.

APPENDIX B: PARAMETERS OF THE γ DOR STARS

We list the observed and TAR fitting parameters of 611 γ Dor stars in this paper. The parameters are: the *Kepler* magnitudes, the effective temperatures, the luminosities, the mode identifications ($k \equiv l - |m|$, l is the angular degree, and m is the azimuthal order), mean pulsation periods $\langle P \rangle$, mean period spacings $\langle \Delta P \rangle$, slopes $\langle \Sigma \rangle$, asymptotic spacings Π_0, near-core rotation rates $f_{\rm rot}$, the ranges of

radial orders n, and ranges of spin parameters s. We also mark the stars which have short-cadence data or have p-mode oscillations. The full version of this table can be found online.

APPENDIX C: RAPIDLY ROTATING STARS WITH ROTATIONAL SPLITTINGS

We find 11 stars that rotate rapidly but still show rotational splittings. These stars are interesting because rotational splittings are rare among rapid rotators. The inclinations of these stars should be very small so the tesseral modes are seen, based on the amplitude distribution theory.

APPENDIX D: SURFACE MODULATIONS OF 58 STARS

58 stars show surface modulation signals. Most of them are caused by the surface activities while a few are classified as eclipsing binaries. Their orbital periods are short hence we assume their surfaces have been tidally locked.

This paper has been typeset from a TEX/LATEX file prepared by the author.